Marine and Petroleum Geology 155 (2023) 106393

Contents lists available at ScienceDirect

Marine and Petroleum Geology

journal homepage: www.elsevier.com/locate/marpetgeo

Movable fluid evaluation of tight sandstone reservoirs in lacustrine delta front setting: Occurrence characteristics, multiple control factors, and prediction model

Dehao Feng [a,b], Chenglin Liu [a,b,*], Xiaolong Feng [c], Xinpei Wang [a,b], Rizwan Sarwar Awan [d], Xiaoyi Yang [a,b], Nuo Xu [a,b], Yunfei Wu [a,b], Yuping Wu [a,b], Qibiao Zang [a,b]

[a] State Key Laboratory of Petroleum Resources and Prospecting, China University of Petroleum-Beijing, Beijing, 102249, China
[b] College of Geosciences, China University of Petroleum-Beijing, Beijing, 102249, China
[c] No.1 Oil Production Plant, Changqing Oilfield Company, PetroChina, Yan'an, 716000, China
[d] School of Resources and Environmental Engineering, Hefei University of Technology, Hefei, 230009, China

ARTICLE INFO

Keywords:
Movable fluid
Nuclear magnetic resonance
Fluid mobility
Pore-throat structure
Tight sandstone
Ordos basin

ABSTRACT

The tight sandstone, deposited in a lacustrine delta front setting, constitutes substantial new petroleum reserves. Tight sandstone reservoirs' fluid mobility directly affects oil production and recovery efficiency. Consequently, it is crucial to quantitatively and synthetically characterize fluid mobility. This study presented a detailed investigation of the movable fluid of the Yanchang tight sandstone in the Ordos Basin. Multiple experiments were conducted to investigate movable fluid, including casting and cathodoluminescence thin section, nuclear magnetic resonance, X-ray diffraction, and high-pressure mercury intrusion. According to pore-throat structure investigation with petrographical observations, delta front sandstone was divided into four types of lithofacies, pore-throat structure, and three pore-throat spaces (nano-scale, submicron, and micron), which correspond to various occurrence characteristics of the movable fluid. The result shows that the fluid mobility of the micron pore-throat space is higher than the sub-micron scale, and the nano-scale is the lowest. The fluid mobility is driven by petrophysical property, pore-throat structure, diagenetic mineral, lithofacies, and sandstone strata pattern. With the deterioration of the pore-throat structure and petrophysical property, fluid mobility gradually decreases. Movable fluid content significantly correlates with quartz and feldspar content, showing that residual intergranular and feldspar dissolved pores can significantly improve fluid mobility. On the contrary, it is negatively correlated with clay and carbonate cement content. The carbonate cementation and clay mineral filling increase the proportion of nano-scale pore-throat, leading to the deterioration of the reservoir quality and pore-throat structure. Detailed researches on the spatial distribution of fluid mobility show it related to sandstone bed thickness, mudstone proximity, and mudstone/formation ratio. Typically, medium-grained sandstones forming thick beds in mudstone-poor sequences are commonly low in carbonate and clay mineral cement and highest in movable fluid content. In contrast, fine-grained sandstones occurring as thin beds or located near the mudstone-sandstone interface in mudstone-rich sequences generally exhibit high carbonate and clay cement. Hence, its movable fluid content is lowest. The frequent material exchange between sandstone and adjacent mudstone prompts the enhancement of the cementation of clay and carbonate minerals, which is a devastating factor for fluid mobility. The proposed model for predicting fluid mobility can be used for similar delta front sandstones of other lacustrine basins. These findings provide new insights into predicting the best reservoir sandstones with high fluid mobility and effectively exploiting tight sandstone reservoirs.

1. Introduction

With the reduction of conventional petroleum reserves, tight reservoirs contribute to the essential new reserves under emerging horizontal drilling and hydrofracture technologies (Clarkson et al., 2012; Zou et al., 2013a, 2013b). Hence, increasing attention was

* Corresponding author. College of Geosciences, China University of Petroleum (Beijing), Beijing, 102249, China
E-mail addresses: lclzgx@126.com, liucl@cup.edu.cn (C. Liu).

https://doi.org/10.1016/j.marpetgeo.2023.106393
Received 5 April 2023; Received in revised form 13 April 2023; Accepted 23 June 2023
Available online 24 June 2023

gradually focused on tight sandstone reservoirs (Jia et al., 2012; Li et al., 2022; Vaisblat et al., 2021). However, effective exploitation of tight reservoirs has some inherent challenges due to the ultra-low permeability (usually less than 1mD), low porosity (generally less than 10%), and complex pore-throat system (Liu et al., 2022b; Nelson, 2009; Zou et al., 2013a).

Petrophysical properties, pore-throat structure, and their control factors are the long-term focus of tight sandstone research (Cui et al., 2022; Li et al., 2023; Nelson, 2009; Shao et al., 2017). Meanwhile, diverse experimental techniques and description parameters were established, such as porosity, permeability, pore morphology obtained from casting thin section (CTS) and scanning electron microscope (SEM), pore-throat structure parameters determined by N_2 adsorption, high-pressure mercury intrusion (HPMI), X-ray computed tomography, neutron scattering, constant-speed mercury intrusion, CO_2 adsorption, and nuclear magnetic resonance (NMR) (Clarkson et al., 2012; Dutton and Loucks, 2010; Lai et al., 2018c; Li et al., 2019a; Qiao et al., 2021; Qin et al., 2021; Schmitt et al., 2016). Recent research shows that the volume or percentage of movable fluid was considered more suitable evaluation parameter than porosity and permeability (Wang and Zeng, 2020; Zang et al., 2022a). The fluid occurring in the tight sandstone is distinguished from bound fluid and movable fluid (Kenyon, 1992; Timur, 1969). The resources with production value in the tight sandstone are movable fluids, directly determining recovery efficiency and the yield of oil wells (Kenyon, 1992; Qu et al., 2022). Previous studies have shown that a single experimental method only reflects limited information about the pore-throat structure and fluid flow and requires a comprehensive evaluation by integrating multiple experimental methods (Krakowska et al., 2018). Through the effective combination of HPMI and NMR experiment, the pore-throat size distribution, connectivity, and the occurrence space of movable fluid can be obtained (Huang et al., 2021; Wu et al., 2022; Zang et al., 2022b), which are of great significance for understanding the fluid mobility. The fluid mobility in different pore spaces is significantly different, and the fluid in tiny pores does not seem easy to flow (Li et al., 2019a, 2019b; Zhang et al., 2022a). Anyhow, a detailed evaluation of movable fluid characteristics is crucial for describing tight reservoirs, which can effectively guide the yield prediction and formulation of production optimization plans.

The tight sandstone deposited in the delta front has been the critical target of petroleum exploration and development in recent years in China, such as Sichuan Basin (Wang et al., 2020b), Songliao Basin (Sun et al., 2015; Xi et al., 2019a), Bohai Bay Basin (Wang et al., 2021), and Oros Basin (Li et al., 2022; Zang et al., 2022b), etc. Due to strong heterogeneity and low recovery efficiency of tight sandstone in the delta front, there are vital technical bottlenecks, such as difficulty in finding economic sweet spot reservoirs (Yang et al., 2022). Few systematic studies evaluated movable fluid in tight sandstone of lacustrine delta front. Previous publications have often focused on the effect of micro-scale parameters on fluid flow capacity, such as petrophysical properties and pore-throat structure (Jiang et al., 2023; Li et al., 2019b; Liu et al., 2022a; Qu et al., 2022; Zang et al., 2022a; Zhang et al., 2022a). The consistent conclusion is that the volume and percentage of movable fluid will decrease with the deterioration of the pore-throat structure. However, physical properties and pore-throat structure are radically driven by sandstone composition and structure, which depends on sedimentation and diagenesis (Bjørlykke, 2014; Morad et al., 2010; Wang et al., 2020b; Xi et al., 2019b). Hence, the limited focus on micro pore throat system limits the prediction of the spatial distribution characteristics of the movable fluid. Only a few publications have focused on the impact of deep-water gravity flow sedimentary environment on fluid mobility. The movable fluid content of deep-water gravity flow sandstone is slightly higher than delta front sandstone (Zang et al., 2022b), and the best fluid mobility consists in coarse to medium sandstone (Dong et al., 2023) and cross-bedded fine-grained sandstone lithofacies (Wang et al., 2020c). However, the delta front setting usually has various lithofacies and sandstone genesis, and occurrence characteristics, multiple controlling factors, and distribution model of movable fluid remain poorly discussed. Hence, it is essential to further comprehensively evaluate the fluid mobility of the delta front sandstone from the macro and micro scales.

This study uses the typical sandstone samples in the delta front of the Chang 8 and Chang 9 members of the Upper Triassic Yanchang Formation in the Ordos Basin to comprehensively evaluate movable fluid characteristics through porosity and permeability test, CTS, CL, XRD, HPMI, and NMR experiments. This study aims to: (a) characterize the pore-throat structure and movable fluid characteristics, (b) Quantitative evaluate multiple controlling factors of fluid mobility, and (c) establish a prediction model for fluid mobility in the delta front setting.

2. Geological setting

The Ordos Basin, located in the North China Craton, central China, is a sizeable petroliferous basin (Fig. 1a). According to the current tectonic morphology, structural characteristics, and basement properties of the basin, the Ordos Basin is divided into six units: Western Margin Thrust Belt, Yimeng Uplift, Tianhuan Depression, Weibei Uplift, Yishan Slope, and Jinxi Fold Belt (Fig. 1b). Abundant fracture and fold were relatively developed at the basin edge, whereas the internal stratigraphic structure of the basin is gentle, and the nasal structure was only developed locally. There was a large paleo lake in the late Triassic, and many rivers and deltas were associated with it. Controlled by the development of fluvial-delta-lacustrine sedimentary systems, more than 1000 m of the Yanchang Formation was deposited, where the basin's most crucial petroleum system was formed (Zou et al., 2019). According to the logging curve, lithology, and oil-bearing characteristics, the Yanchang Formation is distinguished as ten members (Fig. 1d). The sedimentary period of the Chang 7 member was the maximum period of paleo-lake area, so the essential source rock was deposited during this period (Hanson et al., 2007). The sandstone intervals of the Yanchang Formation are chiefly fluvial and delta deposits in the shallow lake setting, which are the main reservoirs (Zou et al., 2013b, 2019). The samples studied in this study were mainly collected from the Chang 8 and Chang 9 member in the Yishan Slope (Fig. 1b-c). The Chang 8 and Chang 9 member are important tight oil reservoirs (Liu et al., 2022b; Zhang et al., 2022b). The oil originated from the Chang 7 source rocks migrated downward into Chang 8 and Chang 9 reservoirs (Hanson et al., 2007).

3. Sample and methods

3.1. Samples

We have observed the cores of the 20 wells in detail. According to the available core description in each well, sandstone, mudstone, and other lithology are divided, and the vertical distribution of lithology has been determined. Sixteen tight sandstone samples were collected from 12 oil wells. The lithology of the samples is mainly medium and fine-grained sandstone, covering most main lithofacies types. Their depths have been adjusted relative to well logs to achieve a correlation of lithological characteristics. Cylindrical plugs with a diameter of 2.5 cm and a length of about 8 cm were drilled along the bedding of cores. Table 1 shows the basic information of 16 studied sandstone samples. All the samples have removed the remaining hydrocarbons and impurities in advance. Seven consecutive experiment testing were conducted on all samples. The small plug with a length of 4 cm in the middle of the cylindrical plug was used for porosity, permeability, NMR, and HPMI experiments. The remaining samples at both ends of the cylinder plug were used for CTS, XRD, and CL.

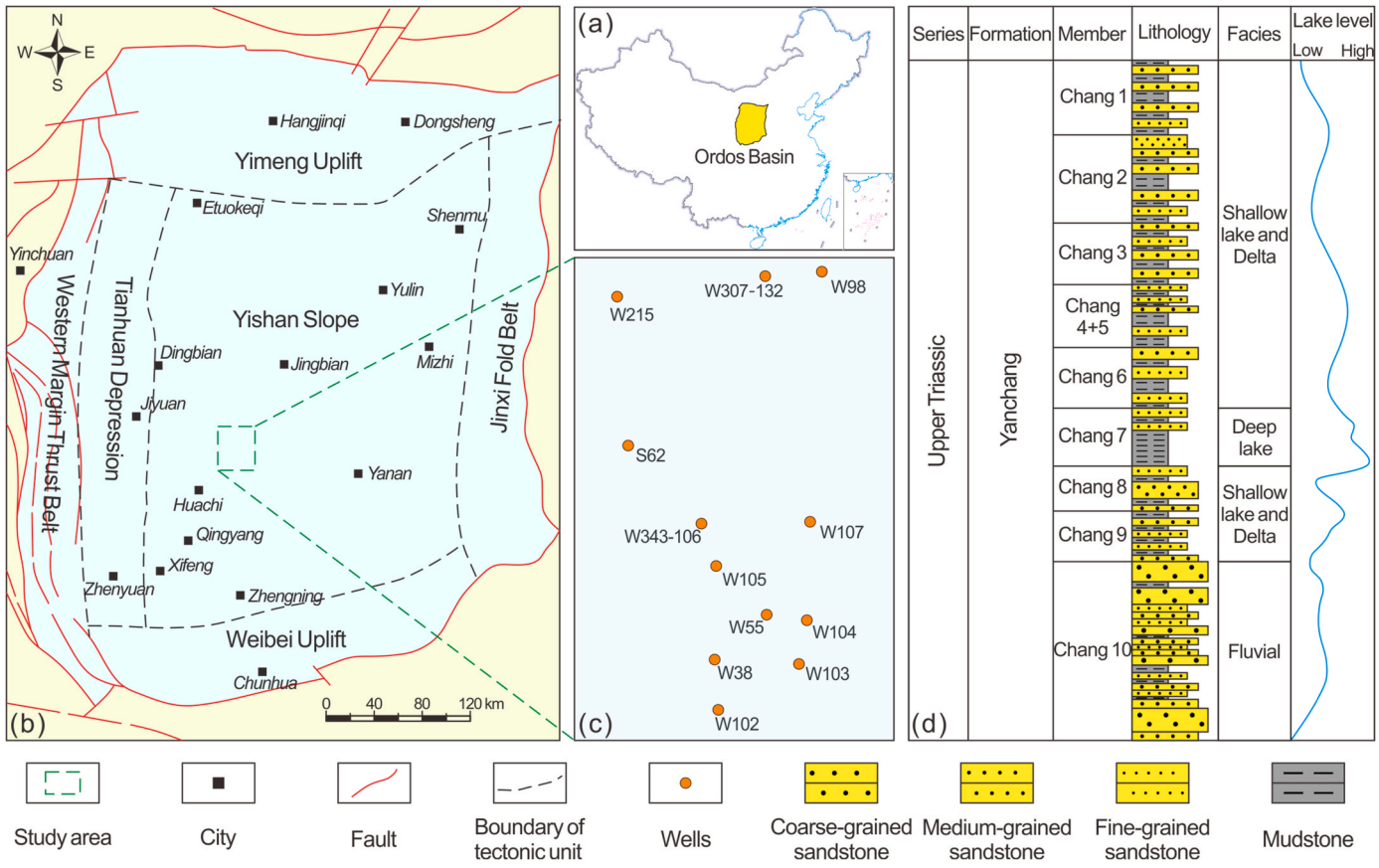

Fig. 1. (a) Location map for the Ordos Basin in China. (b) An overview map of the Ordos Basin, showing six units and the main city. The green box indicates the study area. (c) Location map of the sample wells. (d) The Upper Triassic stratigraphic column showing lithologies and sedimentary facies (Xi et al., 2019b).

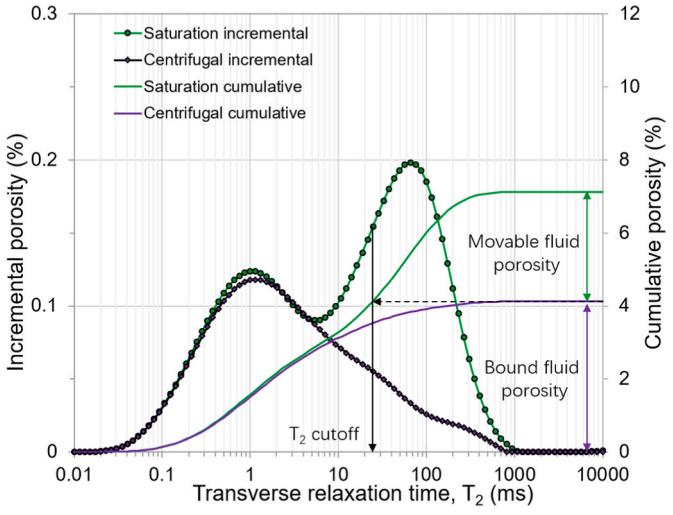

Fig. 2. Schematic diagram of determining T_2 cutoff, P_{mf}, and S_{mf}.

Table 1
Sample information and petrophysical properties of the studied samples in the Yanchang Formation.

Sample	Well	Depth	Porosity (%)	Permeability (10^{-3}μm^2)	RQI
#1	W215	2098.34	8.13	0.085	0.003
#2	S62	2060.77	6.08	0.036	0.024
#3	W343-106	2031.43	11.56	0.038	0.018
#4	W38	2234.33	4.38	0.005	0.011
#5	W307-132	2074.25	7.83	0.075	0.031
#6	W103	2132.63	7.65	0.091	0.034
#7	W38	2329.29	10.63	0.294	0.052
#8	W55	2202.14	2.75	0.001	0.006
#9	W103	2260.99	7.13	0.028	0.020
#10	W102	2264.43	9.17	0.367	0.063
#11	W98	2171.36	9.84	0.104	0.032
#12	W107	2172.23	8.45	0.235	0.052
#13	W107	2169.45	8.29	0.246	0.054
#14	W104	2180.95	7.66	0.024	0.018
#15	W105	2205.1	9.8	0.650	0.081
#16	W105	2196.97	11.59	0.458	0.062

3.2. Experimental methods

3.2.1. Porosity and permeability

The porosity was determined by helium injection using JS 100007 helium porosimeter. This study measured permeability using an A-1013 gas permeameter. Porosity and permeability were measured according to standard technology.

3.2.2. CTS

The mineral and pore morphology characteristics can be directly observed by the casting thin section using an electron microscope (Bjørlykke, 2014; Lai et al., 2018b; Soeder and Chowdlah, 1990). Cut a thin section on the core samples, and then inject the epoxy resin with blue dye into the pore and throat of the thin section. Finally, grind the thickness of the thin section to 0.03 mm. Leica DMLP polarizing microscope was used to observe the prepared casting thin section.

3.2.3. CL

The preparation of a cathodoluminescence thin section is similar to CTS, but the former is slightly thicker. The CL thin sections were conducted on the CL8200MK5-2 cathodoluminescence instrument. Test conditions were 13.5 kV beam voltage and 250 mA beam current.

3.2.4. XRD

Mineral composition and content can be obtained through an X-ray diffraction experiment widely used to study tight reservoirs (Lai et al., 2018b; Wu et al., 2022). Before the test, the sample needs to be crushed to less than 200 meshes and coated on the glass sheet. When measuring the clay mineral contents, it is necessary to separate the clay component from the stable water suspension. The XRD experiment instrument is the D8 DISCOVER instrument.

3.2.5. NMR

NMR experiment testing was carried out on the MARAN-DRX/2 equipment. The experiment consists of a saturation and centrifugation experiment. First, place the tight sandstone sample with impurities and hydrocarbons removed in an oven at 105 °C for 72 h to take out the remaining water. Then, the mass and size of the dried sample were measured. The $CaCl_2$ solution with a salinity of 25,000 ppm was used as NMR experimental liquid. Then, the samples were saturated with experimental liquid for 48 h under 20 MPa saturation pressure, and the mass of samples under saturated water conditions was determined. After sample processing, the transverse relaxation time (T_2) spectrum of samples was determined. After measuring the T_2 spectrum, the samples were centrifuged at 413PSI. Previous studies suggested tight sandstone could lose almost all movable water under the centrifugal pressure of 413psi (Jiang et al., 2019; Zang et al., 2022a). After centrifugation, the T_2 spectrum of the samples was determined. The experiment conditions were set as follows: the test temperature is 35 °C, the echo interval is 0.1ms, the number of scans is 128, the waiting time is 6s, the receiving gain is 80%, and the number of echoes is 16,384.

3.2.6. HPMI

To ensure the consistency of measured samples, the samples after the NMR experiment were used for the HPMI experiment. The samples were dried at 105 °C. The HPMI experiment testing was conducted on Auto-Pore IV 9500 automatic mercury porosimeter. First, the samples were placed in a closed dilatometer for vacuum testing. To ensure that the pore space is not destroyed by mercury, the maximum mercury pressure is set to 200.62 MPa, and the corresponding pore-throat radius is about 3.7 nm. According to the Washburn equation, the relationship between pore-throat radius and mercury pressure is as follows (Washburn, 1921):

$$r = \frac{2\sigma \cos\theta}{P_c} \tag{1}$$

where P_c is the mercury capillary pressure, MPa; r is the pore-throat radius, μm; θ is the wetting angle, 140°; σ is the interfacial tension, 0.48 N/m.

3.3. Analytical theory

3.3.1. Determination of T_2 cutoff and movable fluid

The T_2 cutoff, movable fluid saturation (S_{mf}), and movable fluid porosity (P_{mf}) can be obtained from the T_2 spectrum with saturated water and centrifugal conditions (Gao and Li, 2015; Kenyon, 1992; Testamanti and Rezaee, 2017; Timur, 1969). The T_2 cutoff is the critical value distinguishing bound fluid and movable fluid. The detailed method for determining the T_2 cutoff is shown in Fig. 3. The P_{mf} refers to the difference between the porosity under the saturated water and centrifugal conditions, representing the percentage of pore-throats occupied by movable fluid. The S_{mf} represents the ratio of movable fluid porosity to porosity, indicating the relative size of pore-throat space (Gao and Li, 2015; Zhang et al., 2022a). (see Fig. 2).

3.3.2. Method of transforming NMR T_2 spectrum into pore-throat size distribution

The distribution characteristic of the T_2 spectrum is related to the pore-throat structure, which can directly reflect the pore-throat size distribution (PSD). Therefore, it is necessary to establish a reasonable formula to convert transverse relaxation time into the pore-throat radius. The pore-throat radius obtained from the HPMI experiment on the same sample provides a solution to this problem. Based on the NMR basic theory, the transverse relaxation time is expressed as (Kleinberg, 1999):

$$\frac{1}{T_2} = \frac{1}{T_{2Surface}} + \frac{1}{T_{2Diffusion}} + \frac{1}{T_{2Bulk}} \tag{2}$$

where T_2 is the transverse relaxation time, ms; $T_{2Surface}$, $T_{2Diffusion}$, and T_{2Bulk} are the surface, diffusion-induced, and bulk relaxation time, respectively. The T_2 of the tight sandstone with 100% saturated salt water only depends on the surface diffusion relaxation. Hence, define (Brownstein and Tarr, 1979):

$$\frac{1}{T_2} \approx \frac{1}{T_{2Surface}} = \rho\frac{S}{V} = \rho\frac{F}{r} \tag{3}$$

S/V is the specific surface area of a single pore; ρ is the transverse surface relaxation strength, μm/ms; F is the pore shape factor (Fs = 2 for

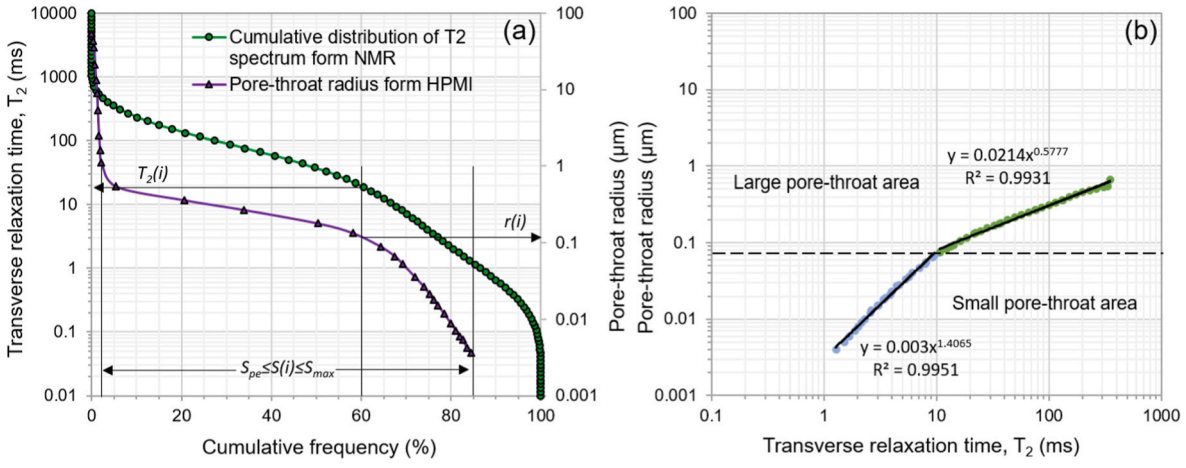

Fig. 3. (a) Schematic diagram of the method of transforming T_2 spectrum into the pore-throat size distribution, and (b) example of obtaining C and n values of sample #1.

cylindrical pores and Fs = 3 for spherical pores). For Eq (3), define:

$$C = \frac{1}{\rho F} \tag{4}$$

Integration Eq (3) and Eq (4), the following formula can be obtained:

$$r = CT_2 \tag{5}$$

However, numerous studies have found non-linear conversion formulas (Wang et al., 2018). Define:

$$r = CT_2^{1/n} \tag{6}$$

where n is a power exponent.

First, plot the pore-throat size distribution determined from the HPMI testing as a cumulative distribution frequency chart. Similarly, the cumulative amplitude percentage of the T_2 spectrum was calculated from the NMR testing. Then, draw both on the same graph according to the same abscissa axis (Fig. 3a). Use the interpolation method to obtain the r(i) value and corresponding $T_2(i)$ under the same saturation (S(i)) between the maximum mercury saturation (S_{max}) and mercury saturation corresponding to the displacement pressure (S_{pe}) (Huang et al., 2020; Li et al., 2015; Wu et al., 2022). Based on Eq (6), constant C and n were obtained using the least square method. The "two-stage" fitting method was applied in this paper (Fig. 3b). That is to say, the pore-throat space was divided into small and large pore-throat for fitting, respectively. It can be seen that the "two-stage" fitting method has a high correlation coefficient ($R^2 > 0.99$).

4. Results

4.1. Mineral, petrological, and sedimentary characteristics

The minerals of the tight sandstone are chiefly composed of quartz, feldspar, calcite, and clay minerals (Table 2). Among them, the feldspar content is the highest, ranging from 36.8% to 72.6% (averaging 52.39%). Specially, The feldspar content of sample #14 is significantly higher than other samples, at 72.6%. The quartz content is between 14.6% and 46.4%, averaging 30.08%. Carbonate minerals exist in the form of cement, mainly calcite, while other carbonate minerals, such as siderite and dolomite, are less abundant. The calcite content of samples varies greatly, and Samples #4 and #8 are rich in carbonate minerals. Similarly, the content of clay minerals shows significant differences, ranging from 6.1% to 15.3%, with an average of 11.3%.

Based on detailed core and casting thin section observations, cathodoluminescence, mineralogical characteristics, and sedimentary structure of sandstone, four lithofacies have been identified in the delta front setting: Medium-grained sandstone with cross, massive or parallel bedding (Ms), Fine-grained sandstone with parallel or cross bedding (Fcs), Fine-grained sandstone with massive bedding (Fms), and fine-grained sandstone with strong carbonate cementation (CFs) (Fig. 4).

Various sedimentary structures such as parallel, massive, and cross bedding can be observed in the lithofacies Ms. Due to the limited samples, the medium-grained sandstone was not further subdivided in this study. Lithofacies Ms have a large particle size, poor sorting, a higher content of quartz and feldspar (Q + F) indicating terrigenous input, and a lower content of clay and carbonate minerals (Fig. 4A–D). Beds formed from lithofacies Ms often occur in thick layers (Fig. 5A), indicating the sedimentary environment of underwater distributary channels near the delta plain with rapid unloading and strong hydrodynamic forces. Lithofacies Fcs have parallel or cross bedding, with better-sorting properties than Lithofacies Ms, but lower Q + F content than Lithofacies Ms (Fig. 4E–H). Lithofacies Fcs were mainly deposited in the lower and middle parts of underwater distributary channels. Fine-grained size means lithofacies Fcs is farther away from the source area than lithofacies Ms. Lithofacies Fms is fine-grained sandstone with massive bedding, good sorting, and relatively low Q + F content (Fig. 4I-L). Lithofacies Fms represent the upper and middle parts of underwater distributary channels (Fig. 5B). Lithofacies CFs are characterized by the highest clay and carbonate content, while their Q + F content is lowest (Fig. 4M-P). Lithofacies CFs were typically deposited in the margin of underwater distributary channels or natural leeve settings. Abundant lithofacies CFs can be observed in the mud-rich environment of thin sandstone and mudstone interbedding (Fig. 5C). Also, siltstone lithofacies represent natural levees or sand sheet deposits, and mudstone lithofacies representing underwater distributary bays. Siltstone and mudstone lithofacies are not exploration targets for tight oil due to their poor petrophysical properties and fluid mobility.

The thickness of sandstone bed in the delta front varies greatly, ranging from a minimum of less than 1 m to a maximum of more than 25 m (Fig. 5). Considering the thickness (Table 2), sandstone beds were divided into thick bed (>8 m), medium bed (4–8 m), and thin bed (<4 m). The thick bed revealed by Well W105 indicate the superposition of multiple underwater distributary channel and mouth bar (Fig. 5A), while medium beds in Well W215 indicate a single stage of underwater distributary channel deposition (Fig. 5B). In Well W55, thin bed sandstones and mudstones were frequently interbedded, representing natural levee, sand sheet, or the margin of underwater distributary channel settings (Fig. 5C).

Table 2
Mineral composition, lithofacies, and sedimentary characteristics of the studied samples in the Yanchang tight sandstone. Abbreviations: T_{ssb}, sandstone bed thickness; D_m, distance from the sand-mudstone interface; M/F-5m, mudstone/formation ratio within a 5 m window; M/F-10 m, mudstone/formation ratio within a 10 m window.

Sample	Quartz (%)	Feldspar (%)	Carbonate (%)	Clay (%)	T_{ssb} (m)	D_m (m)	M/F-5m	M/F-10 m	Lithofacies	Sandstone bed Type
#1	46	39.2	0.9	13.9	4.29	1.44	0.21	0.54	Fms	Medium
#2	35.4	37.4	10.7	15.3	6.10	2.03	0.19	0.39	Fms	Medium
#3	37.7	44.4	2.4	14.7	8.52	3.09	0.00	0.07	Fcs	Thick
#4	33.7	36.8	15.4	14.1	3.70	0.55	0.16	0.25	CFs	Thin
#5	39.2	41.8	6	12.2	2.86	0.19	0.46	0.65	Fcs	Thin
#6	46.4	40	1.8	11	4.81	1.31	0.24	0.34	Fms	Medium
#7	21.6	63.2	2.2	9.9	15.75	1.10	0.20	0.17	Fcs	Thick
#8	25.5	43.8	15.4	15	3.82	0.14	0.27	0.31	CFs	Thin
#9	27.3	60.4	4.2	7.4	17.71	4.66	0.00	0.03	Fcs	Thick
#10	24	63.4	1.8	10.8	17.25	2.19	0.06	0.26	Ms	Thick
#11	30.8	55.8	4.8	7.9	6.75	1.48	0.20	0.35	Ms	Medium
#12	21.9	60.9	3	6.1	25.42	6.04	0.00	0.00	Fcs	Thick
#13	24.8	58.1	2.7	10.3	25.42	3.26	0.00	0.17	Ms	Thick
#14	14.6	72.6	0.4	11.2	7.19	0.52	0.40	0.45	Fcs	Medium
#15	31.1	55.7	3.8	6.6	12.09	3.84	0.00	0.08	Ms	Thick
#16	21.2	64.8	1.5	10.1	12.09	0.12	0.10	0.05	Ms	Thick

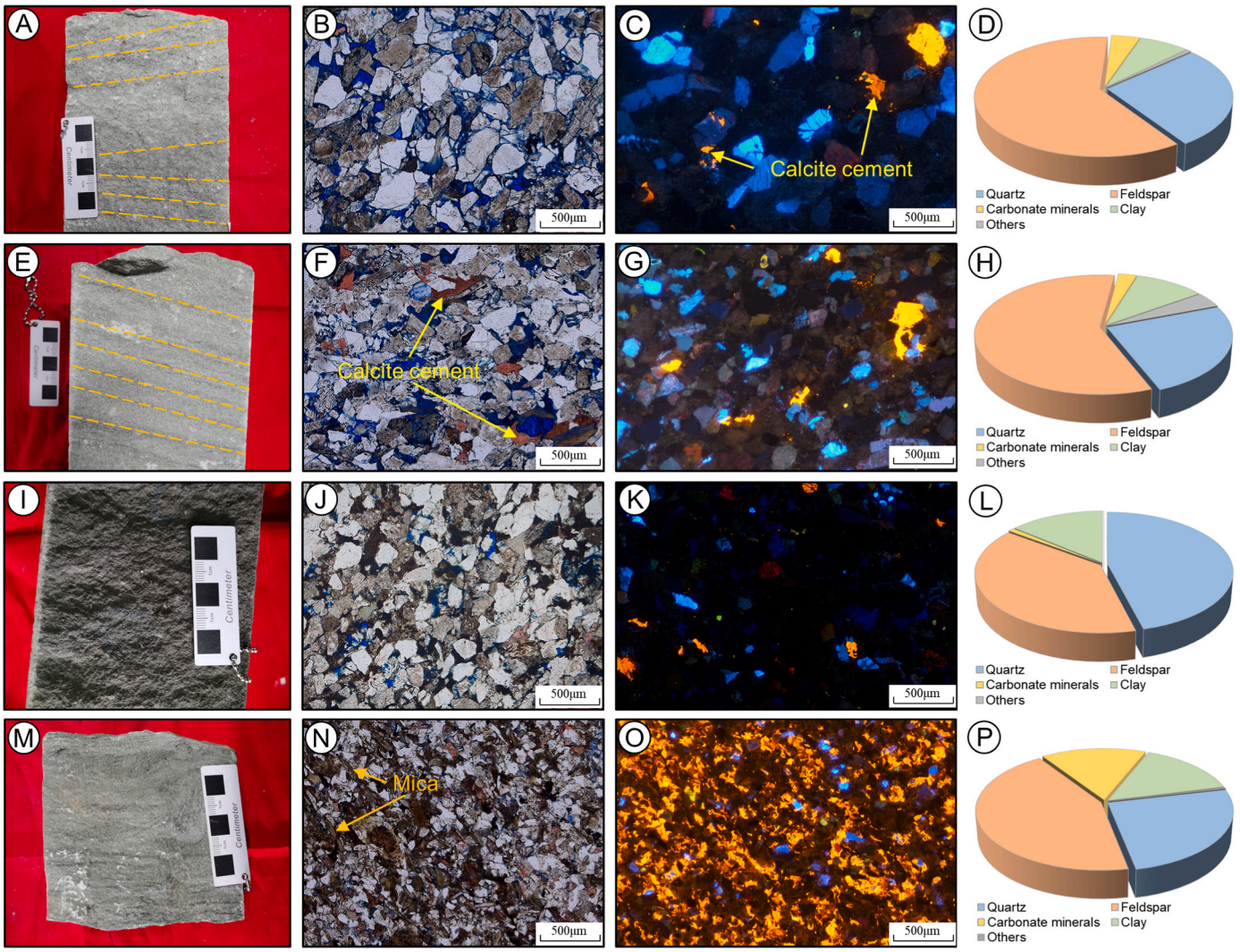

Fig. 4. Lithofacies classification of tight sandstone in the delta front setting based on the core description, casting thin section, cathodoluminescence images, and XRD. (Ã D) Medium-grained sandstone (lithofacies Ms), Sample #13, well W107, 2169.45 m. (E ~ H) Fine-grained sandstone with cross or parallel bedded (lithofacies Fcs), Sample #1, well W215, 2098.34 m. (I ~ L) Fine-grained sandstone with massive bedded (lithofacies Fms), sample #3, well W103, 2260.99 m. (M ~ P) Calcareous fine-grained sandstone (lithofacies Fms), sample #8, well W55, 2202.14 m.

4.2. Reservoir petrophysical properties

The porosity of the tested sandstone samples is between 2.75% and 11.56%, with most distributed between 7% and 9% (Table 1). The permeability varies widely, ranging from $0.005 \times 10^{-3}\mu m^2$ to $0.65 \times 10^{-3}\mu m^2$. Among them, sample #8 has the worst reservoir quality, with a permeability of $0.005 \times 10^{-3}\mu m^2$ and a porosity of only 2.75%.

4.3. Pore-throat structure characteristics

4.3.1. Pore-throat types

Image analyses of CTS showed that tight sandstone reservoirs contain varied types of pores and throats. The pore types include residual intergranular pore, intergranular dissolution pore, intragranular dissolution pore, inter-crystalline pore, and microfracture (Fig. 6). The main throat types include sheet throat, curved sheet throat, and tubular throat. The residual intergranular pore was formed based on the compaction of the primary intergranular pore. The diameter of residual intergranular pores is relatively large, which coexistence with chlorite film can be observed (Fig. 6A). In addition, its edges are relatively straight, and its shape is usually regular (Fig. 6A). Intergranular dissolution pores were often formed by unstable cement (carbonate or turbidite) or feldspar subjected to substantial dissolution, with irregular shapes (Fig. 6B–C). These pores were developed by further enlarging of the residual intergranular pore, and the diameter is generally larger than residual intergranular pore (Fig. 6B). In samples with abundant intergranular dissolution pores and residual intergranular pores, there are often accompanied by sheet throat, curved sheet throat (Fig. 6A–B). Intragranular dissolution pores chiefly exist in feldspar, with relatively small pore diameters and generally filled with clay minerals (Fig. 6D). Inter-crystalline pores with the smallest pore diameter and poor connectivity widely exist in tight sandstone (Fig. 6E). Microfractures are rarely developed, and only a few microfractures can be observed in sample #2 (Fig. 6F). Mica cleavage fractures are also visible in sample #2 (Fig. 6F).

4.3.2. HPMI results

The pore-throat size distribution and capillary pressure curve results of 16 studied samples from HPMI experiments are shown in Fig. 7. Table 3 presents the pore-throat structure parameters. According to HPMI parameters, the morphology of the capillary pressure curve, and pore-throat size distribution, the pore-throat structure of sandstones was divided into four types (i.e., Type I, Type II, Type III, and Type IV). The capillary pressure curve of samples with type I pore-throat structure

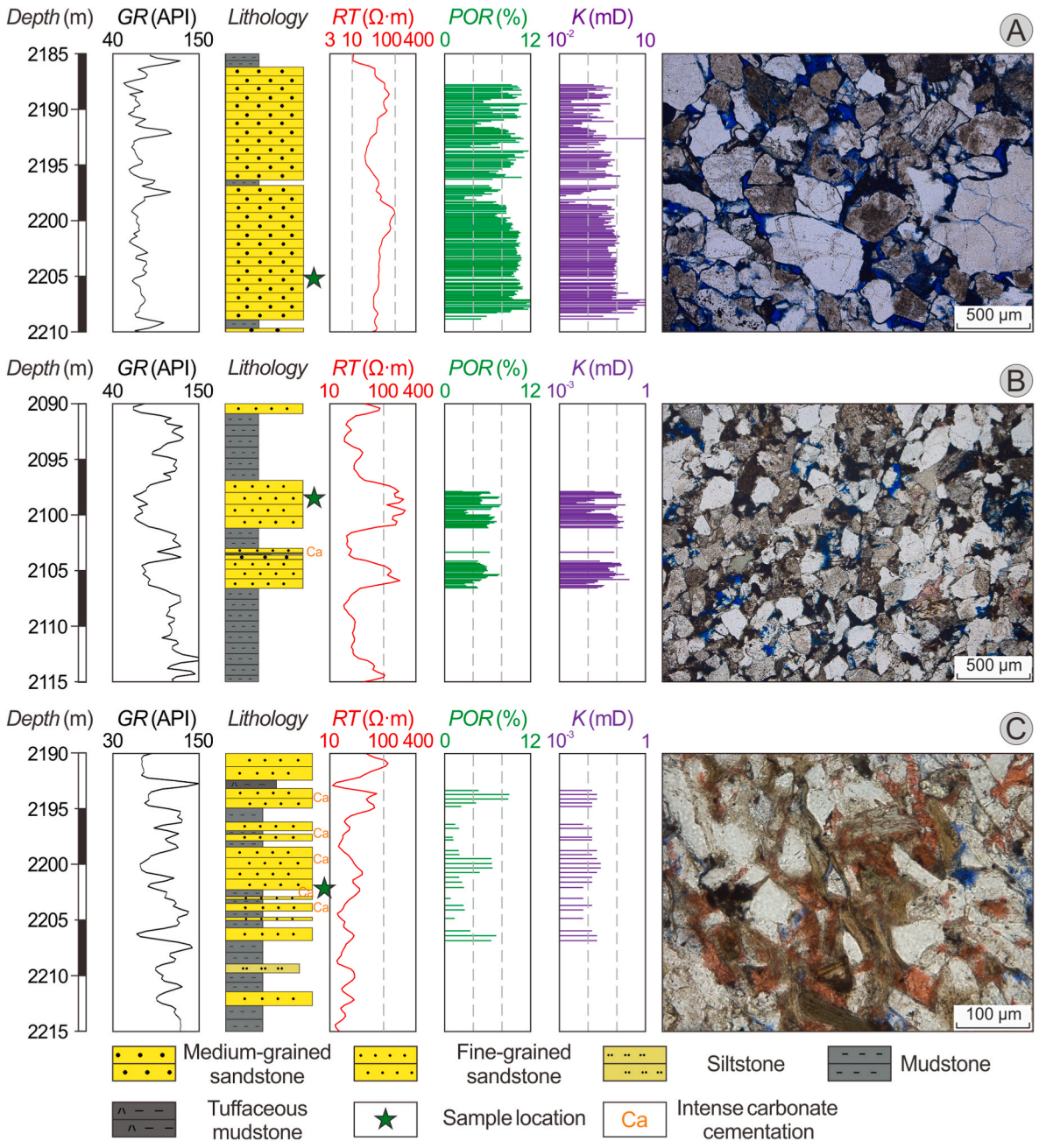

Fig. 5. Typical vertical lithology distribution, showing log curves, porosity, permeability, and photomicrographs of CTS. (A) Thick bed sandstone, Well W105; (B) medium bed sandstone, Well W215; (C) thin bed sandstone, Well W55. Sample locations are shown in a green pentagon.

usually have the lowest platform section and the smallest median pressure (P_{50}, less than 4.07 MPa) and threshold pressure (P_d, less than 0.5 MPa), indicating that such samples have the largest pore-throat size (Fig. 7A). This type have the maximum S_{max} of 85.33% on average, which are the largest among the four types. Type I pore-throat structure's maximum pore-throat radius (r_{max}) is typically greater than 1.5 μm. Additionally, The median and average pore-throat radius (r_a and r_{50}) are the largest, with an average of 0.319 μm and 0.420 μm, respectively. The platform section of type II pore-throat structure is higher than type I, and the corresponding P_d (between 0.66 MPa and 1.36 MPa) and P_{50} (ranging from 4.09 MPa to 5.90 MPa) are both higher than type I (Fig. 7B). The average S_{max} of type II is 81.77%, which is smaller than type I. In addition, The r_{max}, r_a, and r_{50} of type II samples are 0.992 μm, 0.154 μm, and 0.193 μm, respectively, indicating smaller pore-throat development than type I pore-throat structure. For the type III pore-throat structure, the capillary pressure curve has a relatively high platform section (Fig. 7C). The average of P_d and P_{50} are 2.51 MPa and 14.23 MPa, respectively, which are higher than Type II. In addition, the corresponding r_{max} and r_{50} are relatively small, averaging 0.299 μm and 0.054 μm, respectively. Type IV pore-throat structures are characterized by the highest platform section and the lowest S_{max}, indicating the smallest pore-throat size and the worst connectivity (Fig. 7D). From Type I, Type II, Type III to Type IV pore-throat structure, the r_{max}, r_a, and r_{50} indicating the pore-throat size gradually decreases. As the pore-throat structure deteriorates, the mainstream range of the pore-throat radius gradually decreases (Fig. 7E–H).

4.3.3. NMR T_2 spectrum and pore-throat size distribution

Fig. 8 shows the T_2 spectrum of all samples under the fully saturated water state, with T_2 values chiefly ranging from 0.02 ms to 1000 ms. The

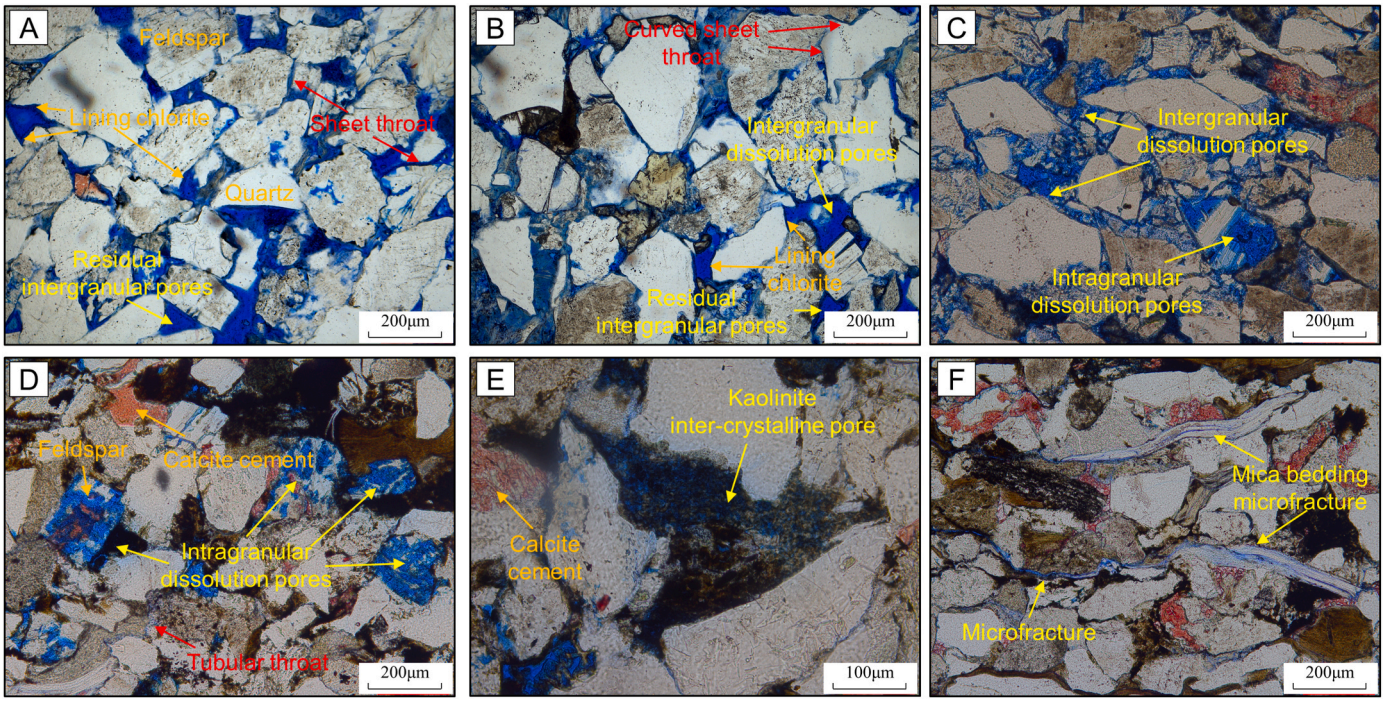

Fig. 6. Pore and throat types determined by CTS analysis. (A) CTS image of sample #11 showing residual intergranular pores with lining chlorite and sheet throats; (B) residual intergranular pores, intergranular dissolution pores, and curved sheet throats (Sample #10); (C) intragranular dissolution pores formed in feldspar and intergranular dissolution pores (Sample #12); (D) intragranular dissolution pores formed in feldspar and tubular throat (Sample #5); (E) inter-crystalline micropores (Sample #2); (F) Microfracture and mica bedding microfracture (Sample #4).

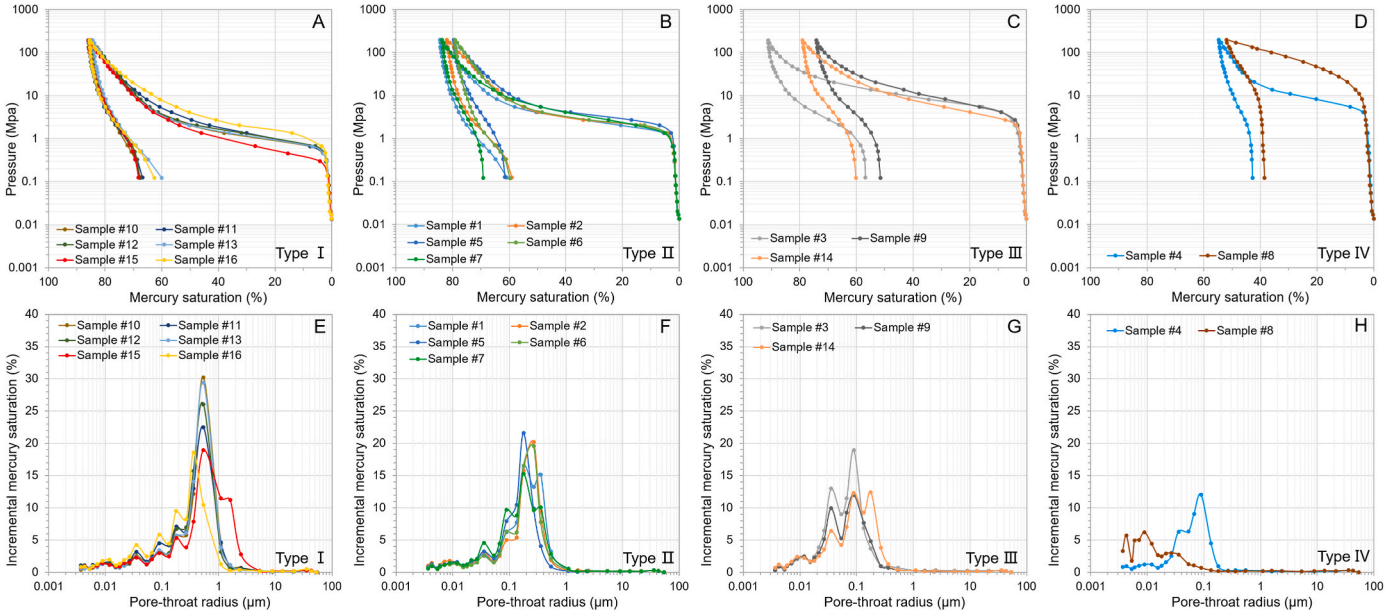

Fig. 7. Four pore-throat structure types of capillary pressure curves (A–D) and pore-throat size distribution (E–H) determined from the HPMI experiment.

T_2 spectrum characteristics vary greatly, showing a unimodal or bimodal morphology, indicating a different pore-throat radius distribution. The T_2 spectrum of most samples (accounting for 75%) are characterized by a bimodal distribution.

Generally, larger T_2 corresponds to larger pore-throat, and smaller T_2 corresponds to relatively more minor pore-throat. However, this is only a qualitative description. Converting the NMR T_2 value into the pore-throat radius is necessary to acquire the PSD. According to the conversion process of Eq. (6) and Fig. 3, the T_2 spectrum of 16 samples were transformed into PSD (Fig. 9). The PSD curve obtained by NMR T_2 spectrum for four types of pore-throat structure have good consistency with the PSD curve obtained by HPMI experiment (Fig. 9A–D), indicating that it is reasonable to transform T_2 spectrum into PSD curve through the "two-stage" fitting method. According to pore-throat, this study divided the pore-throat into nano-scale (radius is less than 0.1 μm), submicron (radius ranges from 0.1 μm to 1 μm), and micron pore-throat (radius is greater than 1 μm).

Porosity contributed by pore-throat of different scales were

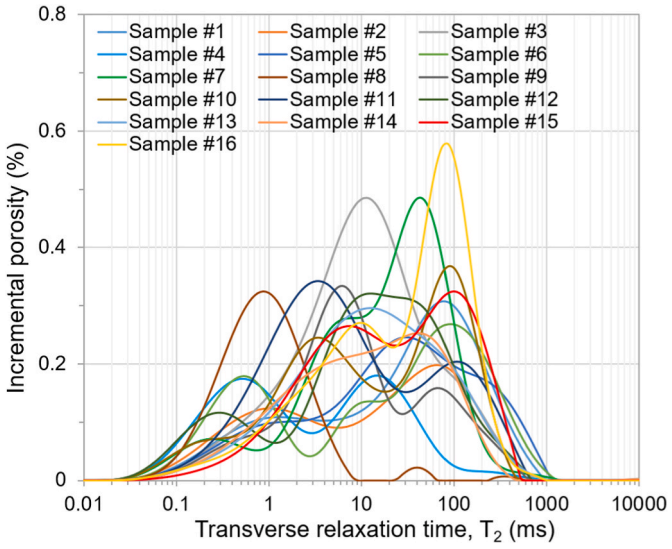

Fig. 8. The T_2 spectrum of 16 studied sandstone samples obtained from the NMR experiment.

calculated based on converted PSD results (Table 4). Consistent with HPMI results, type I pore-throat structures mainly comprise submicron pore-throats and contain some micron pore-throats (Fig. 9E). Type II pore-throat structure samples are also primarily composed of submicron pore-throats. Still, there are no or very few micron pore-throats. Type III and type IV pore-throat structures chiefly consist of nano-scale pore-throats. The proportion of micron and submicron pore-throat from type I to type IV pore-throat structure gradually decreases. In contrast, the proportion of nano-scale pore-throat gradually increases (Fig. 9E).

4.4. Movable fluid characteristics

According to the T_2 spectrum with saturated water and centrifugal conditions, all samples' T_2 cutoff values, S_{mf} and P_{mf}, were calculated according to the process shown in Fig. 3 and Table 3. The S_{mf} can indicate the percentage of movable fluid, whereas the P_{mf} reflects the volume of movable fluid (Gao and Li, 2015; Zhang et al., 2022a). Due to tight sandstone reservoirs' strong inherent heterogeneity, the S_{mf} and P_{mf} show significant differences (Fig. 10). The P_{mf} is between 1.09% and 7.12%, averaging 4.50%. The S_{mf} ranges from 17.93% to 56.83%, with an average value of 44.96%. Except for Samples #4 and #8, the S_{mf} of most samples exceeded 40%.

5. Discussion

5.1. Occurrence characteristics of the movable fluid in different lithofacies and pore-throat structures

Deeply understanding the occurrence characteristics of the movable fluid in different lithofacies and pore-throat structures will be of great significance for hydrocarbon production (Qu et al., 2022; Zang et al., 2022a). The S_{mf} and P_{mf} contributed by pore-throat spaces of different scales are shown in Table 4. Generally, the porosity contributed by the submicron pore-throat space of the Yanchang sandstone is the largest (Fig. 11A), and the movable fluid also mainly occurs in submicron pore-throat space (Fig. 11B–D). The proportion of movable fluid occurring in the submicron pore-throat space of most samples exceeds 70% (Fig. 11D). A few samples, such as Sample #4 and #8, are mainly rich in movable fluids in nano-scale pore-throat. Notably, the proportion of movable fluid occurring in the micron pore-throat of sample #15 exceeds 50%.

For tight sandstone with different pore-throat structures, the occurrence characteristics of movable fluids vary greatly (Fig. 11B–E). The movable fluid of type I pore-throat structure chiefly occurs in submicron and micron pore-throat space, with an average relative proportion of 74.69% and 23.05%, respectively. Micron pore-throats almost only exist in sandstones with type I pore-throat structure and contribute a certain proportion of porosity and P_{mf}. The approximate values of porosity and P_{mf} contributed by micron pore-throat indicate that fluids in micron pore-throat spaces are almost movable. The P_{mf} and S_{mf} of tight sandstones with type II pore-throat structure are almost all contributed by submicron pore-throat, which reflects nearly all movable fluids in submicron pore-throat. Although samples with type II pore-throat structure have a significant proportion of porosity contributed by nano-scale pore-throat (Fig. 11A), the fluids occurring in nano-scale pore-throat spaces tend to be immobile (Fig. 11B–D). The movable fluid of samples with type III pore-throat structure mainly occurs in nano-scale and submicron pore-throat space, with an average relative proportion of 59.25% and 40.69%, respectively. Compared with other types, the movable fluid of the sandstone with type IV pore-throat structure mostly occurs in the nano-scale pore-throat space. The porosity contributed by nano-scale

Table 3
Parameters indicating pore-throat structure and movable fluid of 16 samples derived from the HPMI and NMR experiments. Abbreviations: P_d - Displacement pressure; r_{max} - Maximum pore-throat radius; P_{50} - Median saturation pressure; r_{50} - Median pore-throat radius; r_a - Average pore-throat radius; S_c - Sorting coefficient; S_{max} - Maximum mercury saturation; Φ_{NMR} – NMR porosity; S_{mf} = movable fluid saturation; P_{mf} = movable fluid porosity.

Type	Sample	P_d (MPa)	r_{max} (μm)	P_{50} (MPa)	r_{50} (μm)	r_a (μm)	S_c	S_{max} (%)	Φ_{NMR} (%)	$T_{2cutoff}$ (ms)	P_{mf} (%)	S_{mf} (%)
I	#10	0.48	1.541	2.04	0.360	0.377	2.756	85.35	10.69	8.66	5.88	54.96
	#11	0.46	1.608	2.85	0.258	0.341	2.254	86.00	11.48	8.59	4.87	42.39
	#12	0.47	1.572	2.28	0.322	0.363	2.547	84.87	10.77	10.86	5.66	52.57
	#13	0.46	1.596	2.03	0.362	0.379	2.574	84.39	10.03	10.01	5.37	53.56
	#15	0.14	5.340	1.71	0.430	0.781	2.487	85.81	10.86	15.37	5.85	53.85
	#16	0.46	1.583	4.07	0.181	0.281	2.105	85.57	12.53	20.49	7.12	56.83
	Average	0.41	2.207	2.50	0.319	0.420	2.454	85.33	11.06	12.33	5.79	52.36
II	#1	0.66	1.108	4.09	0.180	0.215	1.789	84.46	9.06	34.80	4.39	48.47
	#2	0.66	1.106	4.20	0.175	0.207	1.900	82.04	7.13	24.47	3.01	42.22
	#5	1.36	0.541	5.90	0.125	0.152	1.713	79.51	8.97	33.24	3.87	43.09
	#6	0.67	1.100	4.49	0.164	0.205	1.700	79.07	9.33	38.96	4.08	43.70
	#7	0.66	1.105	5.81	0.126	0.187	1.799	83.77	11.80	19.71	5.76	48.79
	Average	0.80	0.992	4.90	0.154	0.193	1.780	81.77	9.26	30.24	4.22	45.26
III	#3	2.74	0.268	12.24	0.060	0.067	1.344	91.18	13.11	13.23	5.52	42.12
	#9	2.74	0.268	18.47	0.040	0.069	1.479	74.08	8.38	7.86	3.93	46.87
	#14	2.05	0.359	11.98	0.061	0.100	2.410	78.96	8.72	15.33	3.88	44.49
	Average	2.51	0.299	14.23	0.054	0.079	1.745	81.41	10.07	12.14	4.44	44.50
IV	#4	4.12	0.178	73.78	0.010	0.060	1.503	54.73	6.55	12.41	1.81	27.59
	#8	8.26	0.089	183.81	0.004	0.017	2.108	51.99	6.05	2.00	1.09	17.93
	Average	6.19	0.134	128.79	0.007	0.038	1.806	53.36	6.30	7.21	1.45	22.76

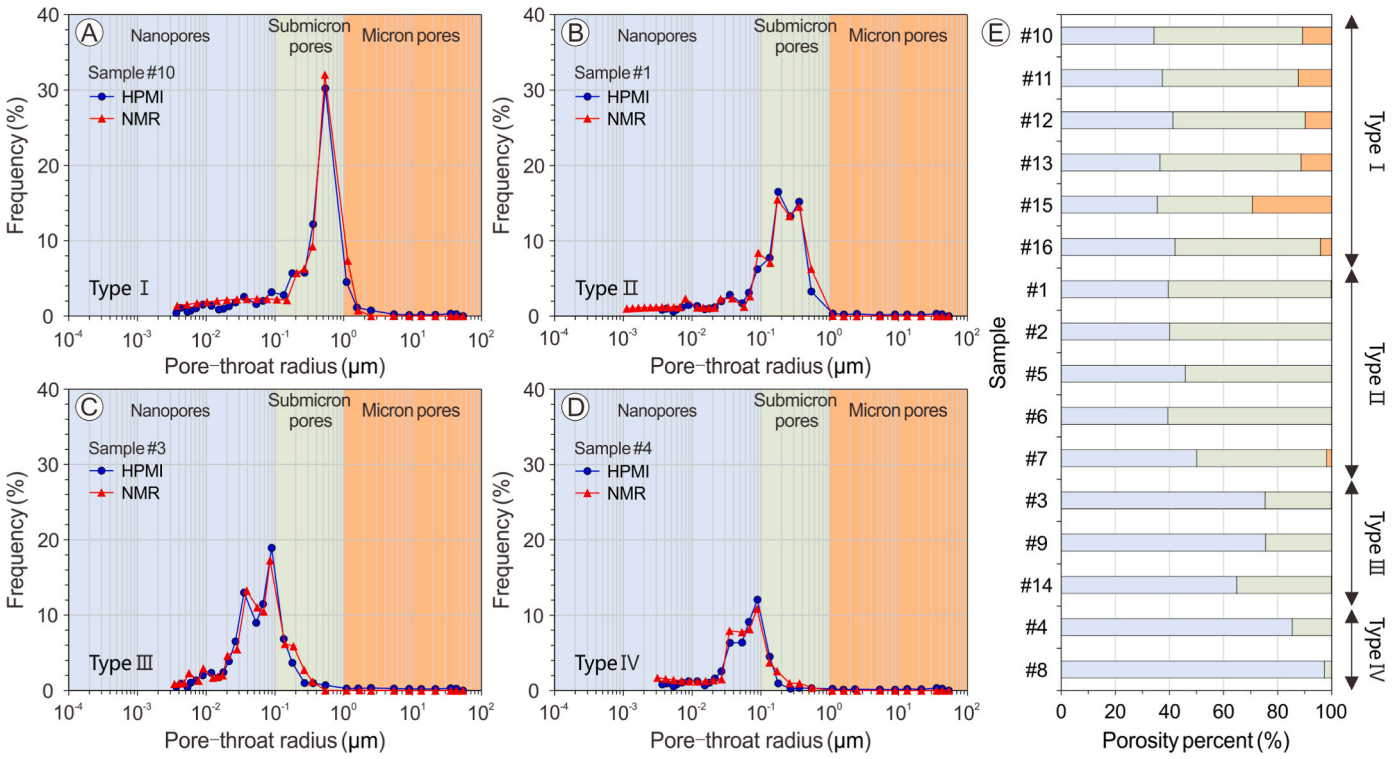

Fig. 9. (A–D) Pore-throat size distributions determined by HPMI and transformed by NMR T_2 spectrum of the different pore-throat structures. (E) The proportion of porosity contributed by pore-throats of different scales.

Table 4
Porosity, movable fluid saturation, and movable fluid porosity of different pore-throat spaces. Abbreviations: Φ_n, Φ_s, and Φ_m - porosity contributed by nano-scale, submicron and micron pore-throat, respectively; MFS_n, MFS_s, and MFS_m - Movable fluid saturation contributed by nano-scale, submicron and micron pore-throat, respectively; MFP_n, MFP_s, and MFP_m - Movable fluid porosity contributed by nano-scale, submicron and micron pore-throat, respectively. MF_n, MF_s, and MF_m - Proportion of movable fluid content contributed by nano-scale, submicron, and micron pore-throat, respectively.

Sample	Nanopore-throat				Submicron pore-throat				Micron pore-throat			
	Φ_n (%)	MFS_n (%)	MFP_n (%)	MF_n (%)	Φ_s (%)	MFS_s (%)	MFP_s (%)	MF_s (%)	Φ_m (%)	MFS_m (%)	MFP_m (%)	MF_m (%)
#1	3.582	0.484	0.044	0.999	5.462	47.817	4.335	98.647	0.021	0.172	0.016	0.354
#2	2.855	1.107	0.079	2.623	4.273	41.083	2.929	97.303	0.002	0.031	0.002	0.074
#3	9.883	19.195	2.517	45.574	3.224	22.867	2.999	54.290	0.008	0.057	0.008	0.136
#4	5.590	19.182	1.256	69.520	0.956	8.410	0.551	30.480	0.000	0.000	0.000	0.000
#5	4.112	2.829	0.254	6.566	4.862	40.260	3.613	93.434	0.000	0.000	0.000	0.000
#6	3.681	0.870	0.081	1.990	5.651	42.831	3.997	98.010	0.000	0.000	0.000	0.000
#7	5.912	2.149	0.253	4.404	5.665	45.563	5.375	93.381	0.220	1.080	0.127	2.214
#8	5.891	17.594	1.065	98.139	0.163	0.334	0.020	1.861	0.000	0.000	0.000	0.000
#9	6.326	25.032	2.097	53.406	2.051	21.840	1.829	46.594	0.000	0.000	0.000	0.000
#10	3.660	3.900	0.417	7.096	5.876	41.203	4.406	74.971	1.158	9.856	1.054	17.934
#11	4.294	0.273	0.031	0.645	5.768	30.945	3.554	72.999	1.422	11.173	1.283	26.356
#12	4.449	0.296	0.032	0.563	5.271	43.396	4.675	82.556	1.054	8.874	0.956	16.881
#13	3.656	0.107	0.011	0.200	5.233	43.467	4.361	81.159	1.143	9.984	1.002	18.641
#14	5.654	13.177	1.150	29.616	3.065	31.266	2.727	70.269	0.004	0.051	0.004	0.115
#15	3.857	0.000	0.000	0.000	3.812	25.880	2.810	48.060	3.190	27.969	3.037	51.940
#16	5.267	2.875	0.360	5.059	6.734	50.223	6.293	88.381	0.529	3.728	0.467	6.560

pore-throat in type I and type II pore-throat structure is relatively small (about 40%), whereas the porosity contributed by nano-scale pore-throat in type III and type IV samples exceeds 60% (Fig. 11A), resulting in lower S_{mf} and P_{mf} and a higher proportion of movable fluid content contributed by nano-scale pore-throat for type III and type IV samples. In addition, the fluid mobility of micron pore-throat space is more elevated than sub-micron scale space, and nano-scale pore-throat space is the lowest.

There are also vast differences in the occurrence characteristics of movable fluids in different lithofacies (Fig. 11). The P_{mf} and S_{mf} of lithofacies Ms are mainly contributed by the submicron and micron pore-throat space. The occurrence characteristics of the movable fluid in lithofacies Fcs vary greatly, but they still primarily occur in submicron pore-throat space. Except for the contribution of submicron pore-throat, movable fluid content of samples #3, #9, and #14 with lithofacies Fcs also have a contribution of nano-scale pore-throat. Almost all movable fluids of lithofacies Fms occurred in submicron pore-throat space, with almost no contribution from micron and nano-scale pore-throat space. The movable fluid of lithofacies CFs mainly exists in nano-scale pore-throat due to the porosity of lithofacies CFs largely contributed by nano-scale pore-throat (Fig. 11A–D; Fig. 11F).

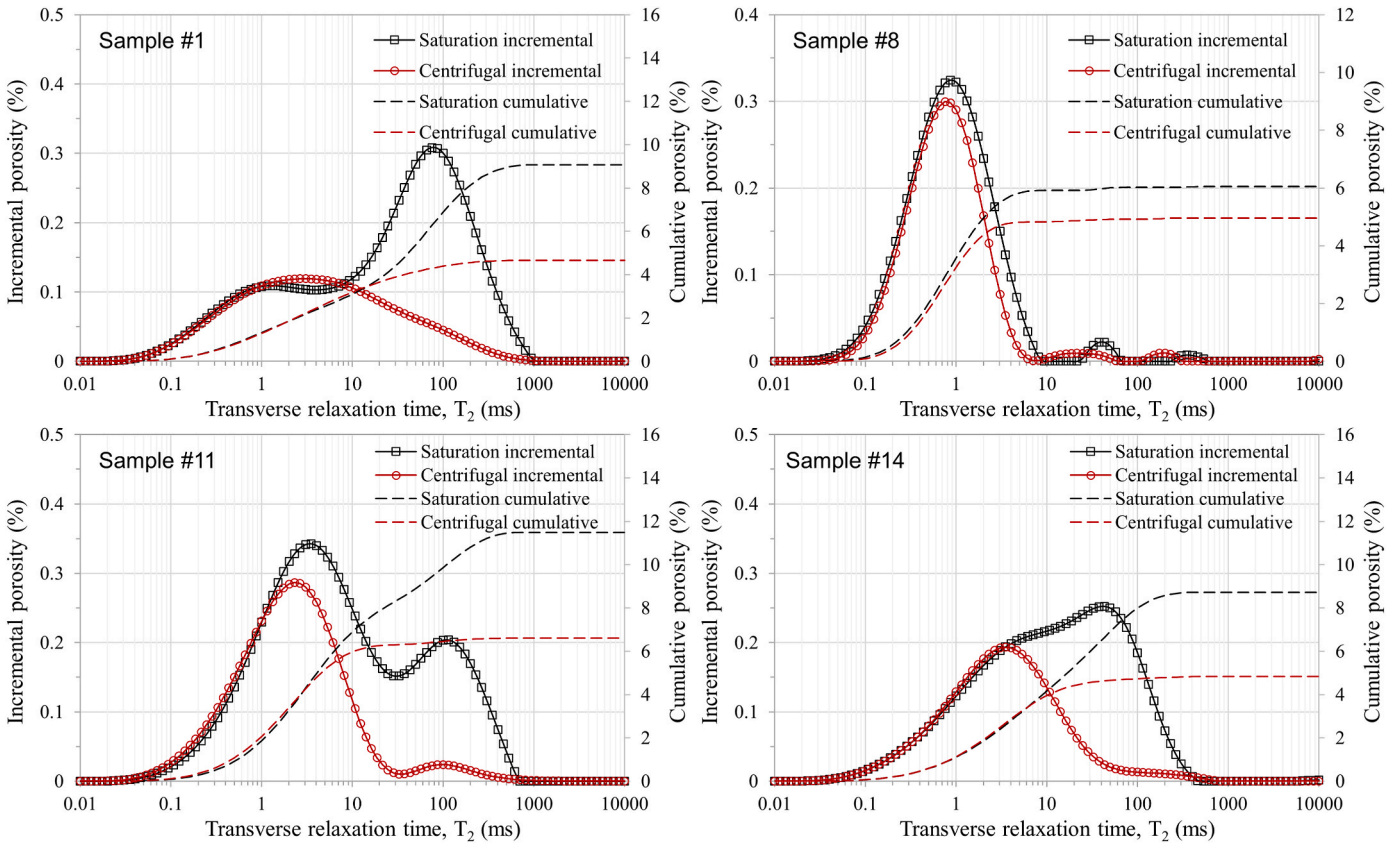

Fig. 10. Typical NMR T_2 spectrum under saturated water and centrifugal conditions for evaluating movable fluid characteristics.

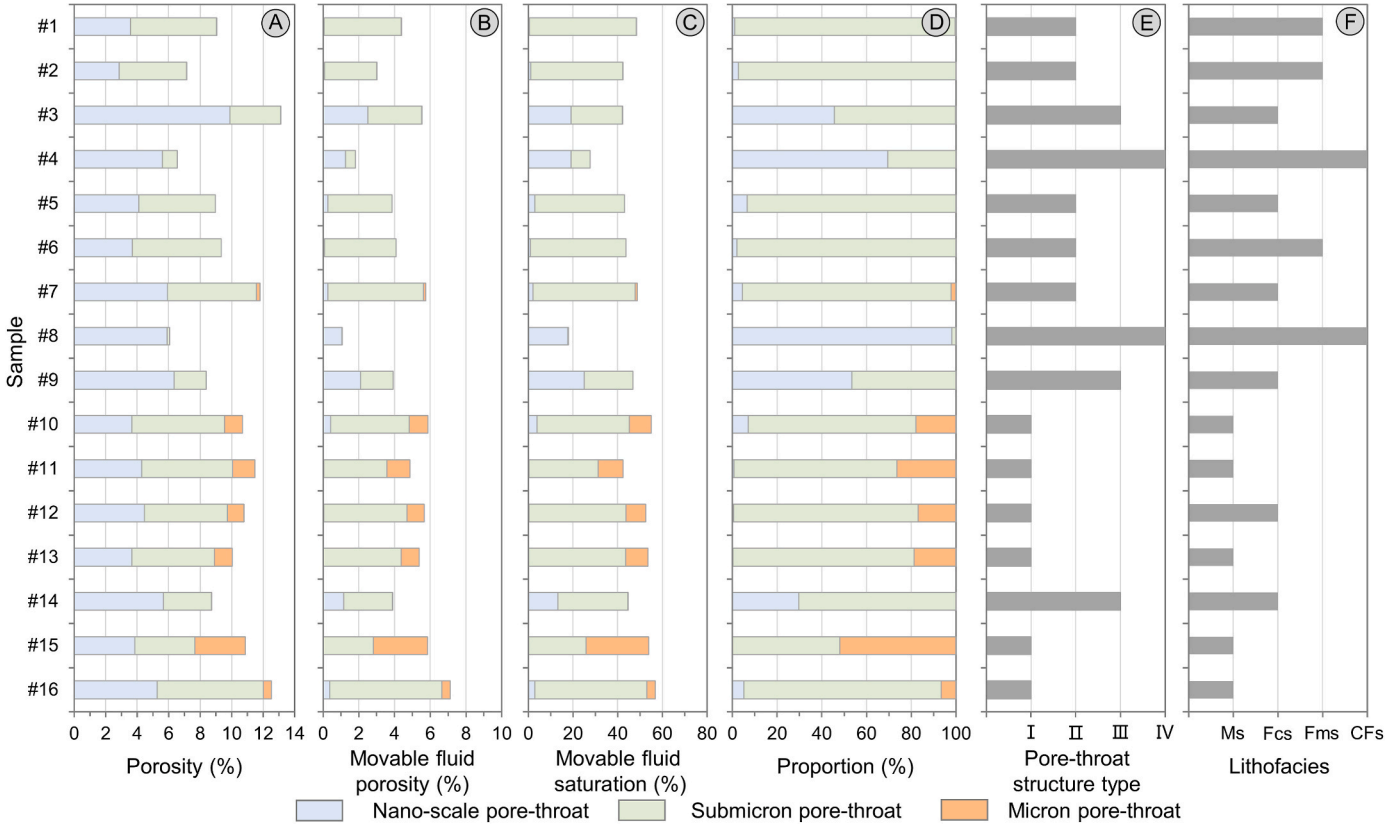

Fig. 11. Porosity (A), P_{mf} (B), S_{mf} (C), and the proportion of movable fluid content (D) contributed by different pore-throat spaces with varying types of pore-structure (E) and lithofacies (F).

5.2. Multiple control factors of fluid mobility in lacustrine delta front setting

5.2.1. Petrophysical property

Porosity, permeability, and reservoir quality index (RQI = $0.0314\sqrt{\frac{\text{Permeability}}{\text{Porosity}}}$) can comprehensively reflect reservoir quality and have been widely used in reservoir evaluation (Sen et al., 2021). Pearson correlation analysis of physical properties and parameters indicating fluid mobility shows that fluid mobility positively correlates with porosity, permeability, RQI, and fluid mobility, with the Pearson correlation coefficient mostly greater than 0.7 (Fig. 12A). Despite all this, having only high porosity may mean high P_{mf}, but it may not necessarily have high S_{mf}. For example, Sample #3 has a permeability and porosity of 0.038mD and 11.56%, respectively, but its P_{mf} and S_{mf} are 5.52% and 42.12%, respectively. Thus, it is necessary to evaluate physical properties to predict fluid mobility comprehensively. The relationship between S_{mf} contributed by different pore-throat spaces (MFS_n, MFS_s, and MFS_m) and physical properties indicates that physical properties are negatively correlated with S_{mf} contributed by nano-scale pore-throat space (MFS_n) and positively correlated with S_{mf} contributed by submicron (MFS_s) and micron pore-throat space (MFS_m). Permeability and RQI have a strong positive correlation with the MFS_m, with Pearson correlation coefficients of 0.79 and 0.75, respectively. In addition, the proportion of porosity contributed by nano-scale pore-throat space (Pcn) has a significant negative correlation with P_{mf} and S_{mf}. In contrast, the proportion of porosity contributed by submicron (Pcs) and micron pore-throat space (Pcm) has a positive correlation with P_{mf} and S_{mf} (Fig. 12A). This further confirms that when the proportion of nano-porosity is large, it will lead to poor fluid flow ability.

5.2.2. Pore-throat structure

Comparing samples with different pore-throat structures, sandstones with type I pore-throat structure generally have the largest P_{mf} and S_{mf}, averaging 5.79% and 52.36%, respectively (Fig. 11). The presence of micron pore-throats are a typical feature of sandstone with type I pore-throat structure, indicating that it can improve the fluid mobility. The P_{mf} of type II pore-throat structure ranges from 3.01% to 5.76%, averaging 4.22%, while the S_{mf} ranges from 42.22% to 48.79%, averaging 45.26%. The P_{mf} and S_{mf} of type III pore-throat structure are similar to

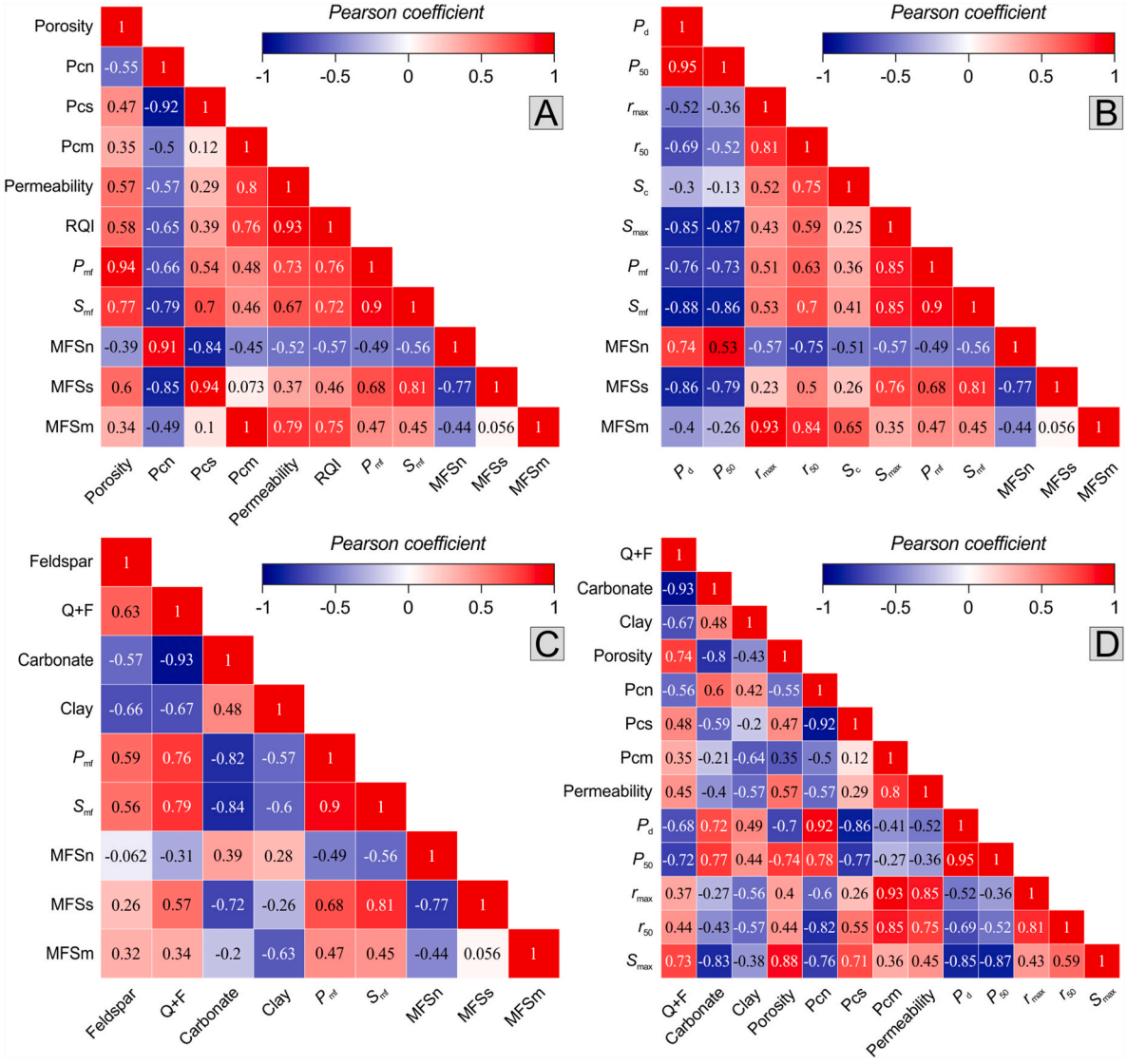

Fig. 12. Pearson correlation matrix of multiple control factors affecting fluid mobility: (A) Petrophysical property, (B) Pore-throat structure parameters, and (C) Diagenetic mineral. (D) Pearson correlation matrix of diagenetic minerals with reservoir quality parameters. Abbreviations: Pcn, Pcs, and Pcm - the proportion of porosity contributed by nano-scale, submicron, and micron pore-throat, respectively; MFS_n, MFS_s, and MFS_m - Movable fluid saturation contributed by nano-scale, submicron and micron pore-throat, respectively; RQI - Reservoir quality index.

type II, with the average values of P_{mf} and S_{mf} being 4.44% and 44.50%, respectively. Tight sandstones with type IV pore-throat structure have the lowest P_{mf} and S_{mf}, averaging 1.45% and 22.76%. Overall, from type I, type II, type III, and type IV, the fluid mobility gradually decreases with the deterioration of the pore-throat structure (Table 3). However, some samples do not follow this trend, which may be related to other control factors. In addition, there is no significant difference in fluid mobility between type II and type III pore-throat structure. The P_{mf} and S_{mf} of sample #11 are relatively low, which is significantly different from other type I samples. The P_{mf} of sample #2 is relatively low, which seems inconsistent with the typical characteristics of type II pore-throat structure (Fig. 11B–D).

Pearson correlation analysis of pore-throat structure parameters with P_{mf} and S_{mf} indicates that pore-throat size and connectivity strongly control fluid mobility (Fig. 12B). The fluid mobility negatively correlates with P_d and P_{50}. The R_{max} and R_{50} indicating the pore-throat size positively correlate with the P_{mf} and S_{mf}, with correlation coefficients generally greater than 0.5. Tight reservoirs with larger pore-throat size typically correspond to higher P_{mf} and S_{mf}. Further, pore-throat size negatively correlates with MFS_n and positively correlates with MFS_s and MFS_m (Fig. 12B). This further confirms that the larger the pore-throat radius, the more movable fluid tends to occur in the submicron and micron pore-throat space, resulting in stronger fluid mobility. The maximum mercury saturation reflects the connected pore-throat volume (Lai et al., 2018a). The S_{max} positively correlates with both P_{mf} and S_{mf} (the Pearson correlation coefficients are all 0.85), indicating that pore-throat connectivity strongly controls the fluid mobility of tight sandstone. The sorting coefficient (S_c) has a weak positive correlation with fluid mobility, inconsistent with previous publications (Zang et al., 2022a; Zhang et al., 2022a). The S_c represents the uniformity of pore-throat radius distribution (Lai et al., 2018c). This research shows that even the more uniform the pore-throat size, it does not necessarily correspond to higher fluid mobility. This conclusion reflects the complex control of reservoir heterogeneity on fluid mobility. In any case, large pore-throat size and better connectivity typically contribute to higher movable fluid porosity and saturation.

5.2.3. Diagenetic mineral

Fig. 12C shows the correlation between mineral compositions and movable fluid parameters. The P_{mf} and S_{mf} have a strong positive correlation with the sum of quartz and feldspar contents while negatively correlated with carbonate and clay mineral contents, reflecting the strong control of diagenetic minerals on fluid mobility. Carbonate cementation has a stronger effect on reducing fluid flow capacity than clay minerals. In addition, carbonate and clay minerals can reduce MFS_s and MFS_m, and increase MFS_n. Brittle mineral particles are susceptible to static rock pressure, and their resist compressive properties are conducive to retaining intergranular pores (Ajdukiewicz and Larese, 2012).

In contrast, ductile clastic minerals are prone to compaction under the overlying stress, which will reduce or disappear intergranular pores (Dutton and Loucks, 2010; Lai et al., 2018b). Pearson correlation analysis of diagenetic mineral content with petrophysical properties and pore-throat structure indicates that the carbonate cementation and clay mineral filling reduce porosity and permeability, leading to the deterioration of the pore-throat structure and reservoir quality and further inhibiting the enrichment of movable fluid (Fig. 12D). Specifically, carbonate cement are crucial for reducing porosity, while clay minerals have a stronger effect on reducing permeability. This may be related to the fact that some clay minerals, such as chlorite, can inhibit compaction and retain intergranular pores (Ajdukiewicz and Larese, 2012; Lai et al., 2018b). Carbonate and clay cement fill pore and throats, decreasing pore-throat size, especially a significant increase in the proportion of nano-scale pore-throats (Fig. 12D). The correlation between carbonate and clay mineral content and S_{max} indicate that cement can reduce the pore-throat connectivity.

5.2.4. Sedimentary environment

Comparing the fluid mobility of different lithofacies, lithofacies Ms has the best fluid mobility, followed by Fcs and Fms, and lithofacies CFs have the worst fluid mobility (Fig. 13A–B). Lithofacies Ms have high porosity, high permeability, and the best type I pore-throat structure. In contrast, lithofacies CFs always have low porosity and permeability, as well as a bad type IV pore-throat structure (Fig. 13C–D). Compared to lithofacies Fms, lithofacies Fcs have a more extensive distribution range of porosity and permeability and a more complex pore-throat structure.

To quantitatively describe tight sandstone's sedimentary environment, this study leads into the sandstone bed thickness, distance from the sand-mudstone interface, and mudstone/formation ratio (M/F ratio). M/F ratio refers to the proportion of mudstone within a 5 m or 10 m sliding window. The closer the M/F ratio is to 1, the greater the thickness of mudstone within this window, indicating a mudstone-rich environment (Table 2). The calculation principle of the M/F ratio is similar to wireline logging, which calculates the proportion of mudstone within the sliding window with the sample depth as the midpoint (Miocic et al., 2020).

The fluid mobility is correlated with the sandstone bed thickness, distance from the sand-mudstone interface, and M/F ratio (Fig. 14). Thick bed sandstone usually has the highest P_{mf} and S_{mf} (Fig. 14A). As sandstone bed thickness decreases, the fluid mobility also reduces significantly. Thin bed sandstone has the lowest fluid mobility. In addition, the P_{mf} and S_{mf} of tight sandstone increase as the distance from the adjacent sand-mudstone interface increases (Fig. 14B). Regardless of the distance from the sand-mudstone interface, lithofacies Ms typically have high fluid flow capabilities. However, the lowest P_{mf} and S_{mf} are usually found near the sand-mudstone interface in fine-grained sandstone lithofacies. A possible explanation is that the M/F ratio may play a role in this variation, as high M/F ratio are limited to low P_{mf} and S_{mf}, and only low M/F ratio extend to high P_{mf} and S_{mf} (Fig. 14C–D). Tight sandstone with high carbonate and clay cement content are typically thin bed or located near the sand-mudstone interface (Fig. 15). Tight sandstone forming in mudstone-rich sequences commonly exhibit strong carbonate and clay cement, which significantly reduce reservoir quality, worsen pore-throat structure, and increase the content of nano-scale pore-throat, leading to the deterioration of fluid mobility.

Many previous works have documented carbonate cementation in sandstones to be related to sandstone-mudstone transition, with stronger cementation occurring near mudstones (Cao et al., 2023; Ma et al., 2019; Miocic et al., 2020; Morad et al., 2010; Wang et al., 2020a; Xi et al., 2019b). Large-scale and frequent mass transfer between tight sandstone and adjacent mudstone are closely related to cementation in the Yanchang Formation (Lai et al., 2017; Xi et al., 2019b; Yang et al., 2022). During diagenesis, depending on the diagenetic mineral reactions in adjacent mudstones, such as carbonate mineral dissolution and smectite-to-illite transformation, ions forming cement enter the sandstone under diffusion and compaction flows (Ma et al., 2019; Thyne, 2001; Yang et al., 2022). Thick bed sandstone would exhibit better reservoir quality and fluid mobility than medium and thin bed sandstone for the abovementioned reason. In mudstone-rich sequences, more diagenetic fluid was expelled from the adjacent mudstones and entered the surrounding sandstone, resulting in strong cementation.

5.3. Prediction model of fluid mobility in the lacustrine delta front setting

The control factors driving fluid mobility in the Yanchang tight sandstones are the depositional environment and diagenesis, which controls the reservoir quality and pore-throat structure. The reliability of predicting fluid mobility through multiple controlling factors largely depends on the reliability of the depositional model. The study area is located in a delta-front setting. The evolution of the lake and delta created a complex alternation of facies, making the prediction of fluid mobility particularly challenging. Consequently, this study established a prediction model of fluid mobility for the lacustrine delta front setting

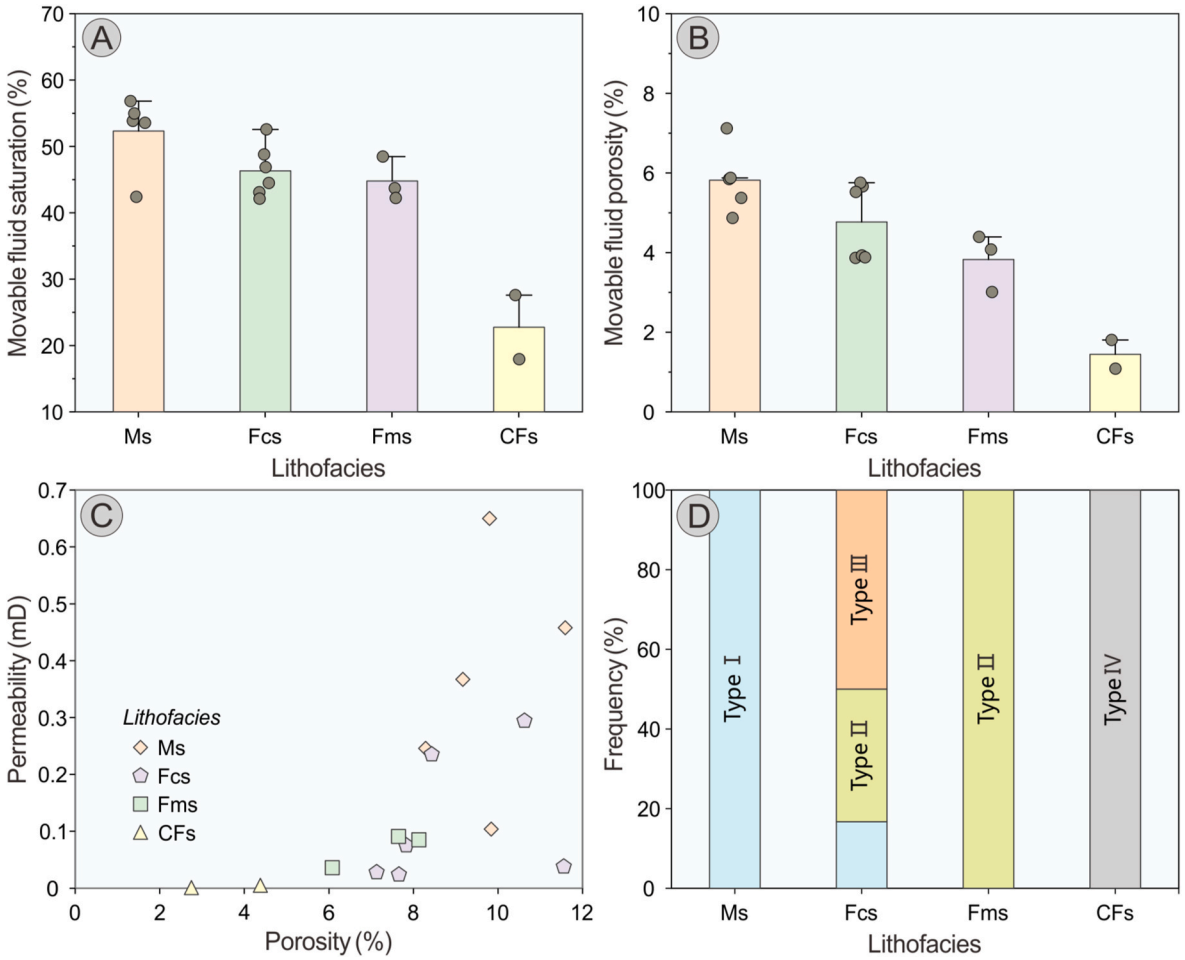

Fig. 13. Bar chart of P_{mf} (A) and S_{mf} (B) with different lithofacies; (C) Scatter diagram of petrophysical properties with different lithofacies; (D) Frequency of pore-throat structure types with different lithofacies.

based on movable fluid's occurrence characteristics and control factors (Fig. 16).

The best fluid mobility mainly occurs in medium-grained sandstone with thick bed, followed by fine-grained sandstone with thick and medium bed. In contrast, the worst fluid mobility commonly occurs in fine-grained sandstone with thin bed or located near the adjacent mudstone. According to the genesis interpretation of the typical braided-river delta front setting, thick bed sandstone is usually formed by the superposition of multi-phase underwater distributary channels and mouth bar (Fig. 16B1 and C1). In the delta front setting, medium-grained sandstone lithofacies is generally closer to the source area than fine-grained sandstone lithofacies. Residual intergranular pores commonly dominate medium-grained sandstone owing to the high content of quartz and feldspar (Fig. 16B2). These lithofacies have the largest pore-throat size, best pore-throat connectivity, and highest permeability and porosity, resulting in the best fluid mobility (Fig. 16B3). The genesis of fine-grained sandstone with thick bed is similar to medium-grained sandstone with thick bed, but the former is closer to the lake center in comparison. This type of sandstone deposit is mainly characterized by the development of residual intergranular and intragranular dissolution pores, with submicron pore-throat size, medium connectivity, and petrophysical properties dominated, leading to medium fluid mobility (Fig. 16C2–C3). Fine-grained sandstone with medium bed represents single-stage underwater distributary channel or mouth bar deposits (Fig. 16D1). It mainly comprises sandstones far from the source area, developing intergranular dissolution pores and little intergranular pores (Fig. 16D2). Similar to fine-grained sandstone with thick bed, fine-grained sandstone with medium bed generally has medium fluid mobility (Fig. 16D3). Due to strong cementation in the fine-grained with thin bed or top and bottom location of thick and medium bed, nano-scale pore-throats are chiefly developed in these sandstone deposits (Fig. 16E1-E2). Poor reservoir quality and pore-throat structure lead to a lack of movable fluid (Fig. 16E3). Hence, a good knowledge of the depositional model, particularly lateral and vertical variation of mudstone and sandstone, is essential for using the prediction model.

6. Conclusion

The tight sandstone deposited in the lacustrine delta front setting contributes to many new oil and gas reserves. Movable fluid evaluation is crucial in reservoir characterization, as it directly affects oil production and recovery efficiency. However, fluid mobility prediction of delta front sandstone has inherent challenges due to strong heterogeneity, complex pore-throat system, and alternation of facies. Hence, this integrated work conducts multiple experiments to investigate the occurrence, control factors, and prediction of the spatial distribution of movable fluid.

The fluid mobility of micron pore-throat space is highest, followed by sub-micron pore-throat, whereas nano-scale pore-throat is the lowest. Generally, the movable fluid of the delta front sandstone mainly occurs in submicron pore-throat space. The fluid mobility is strongly controlled by petrophysical properties and pore-throat structure. The carbonate cementation and clay mineral filling increase the proportion of nano-scale pore-throat, leading to the deterioration of the pore-throat

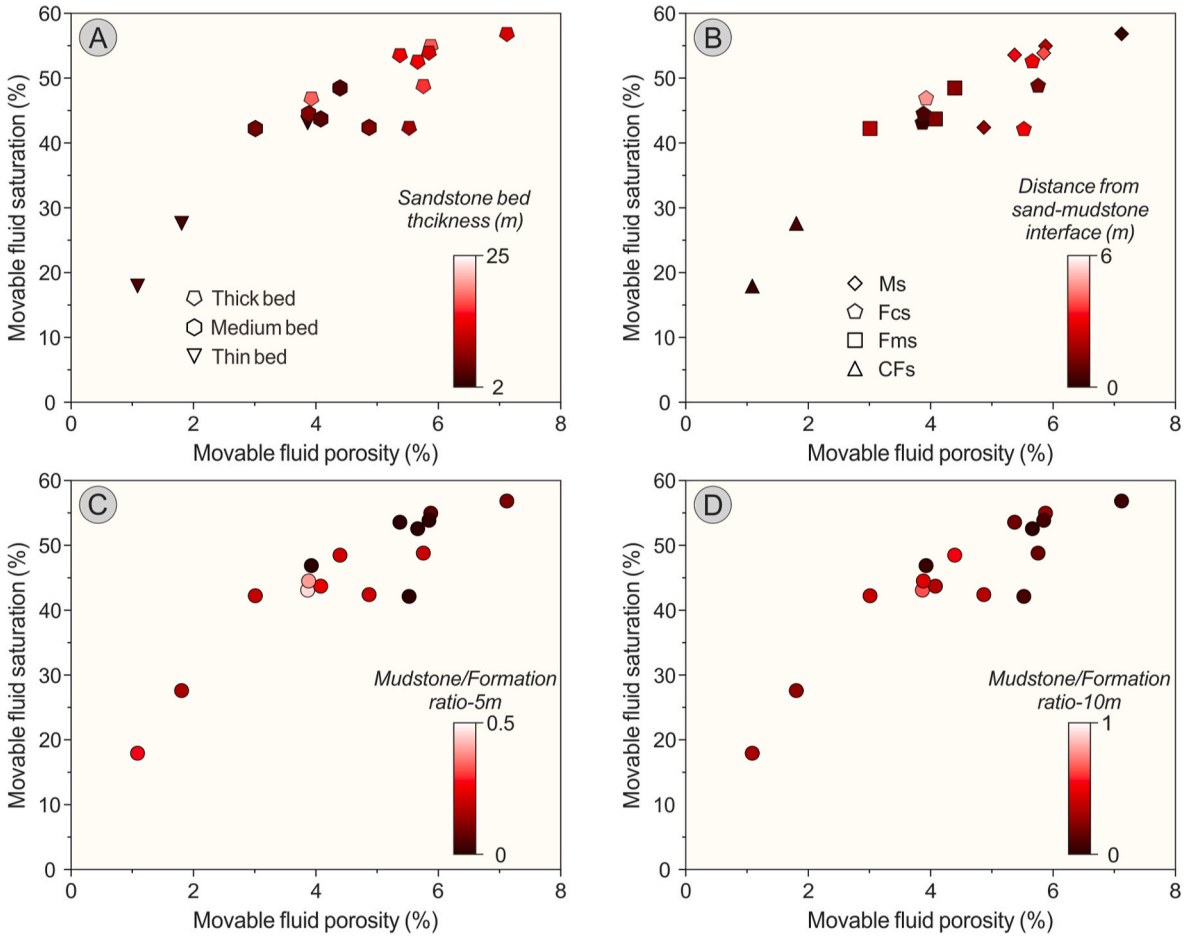

Fig. 14. Plot illustrating porosity-permeability vs. (A) Sandstone bed thickness, (B) Distance from the adjacent sand-mudstone interface with different lithofacies, (C) Mudstone/Formation ratio-5m, and (D) Mudstone/Formation ratio-10 m.

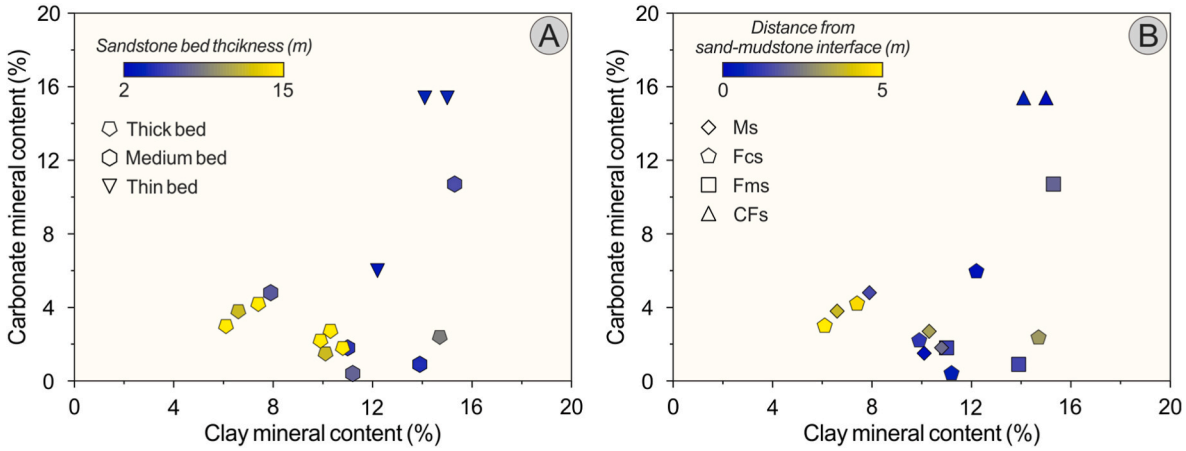

Fig. 15. Corss-plot of carbonate cement content vs. clay mineral content. Plot illustrating the influence of the sandstone bed thickness (A) and distance from the adjacent sand-mudstone interface with different lithofacies (B) on carbonate and clay cement content.

structure and reservoir quality. Lithofacies and sandstone strata patterns control petrophysical properties and pore-throat structure by influencing diagenesis, resulting in differences in fluid mobility.

Based on the above results, this study established a prediction model for fluid mobility in the lacustrine delta front setting. The best fluid mobility occurs in medium-grained sandstones with thick bed, followed by fine-grained sandstone with thick and medium beds. In contrast, the worst fluid mobility commonly occurs in fine-grained sandstone with thin bed or located near the adjacent mudstone. The reliability to predict fluid mobility of the tight sandstone in the lacustrine delta front setting require the precision of the depositional model, particularly spatial variation of mudstone and sandstone.

This study emphasizes the movable fluid evaluation of tight sandstone in the delta front from both macro and micro scales. The proposed model for predicting fluid mobility can promote the effective exploitation of tight reservoirs. Furthermore, it can be used as a methodology in

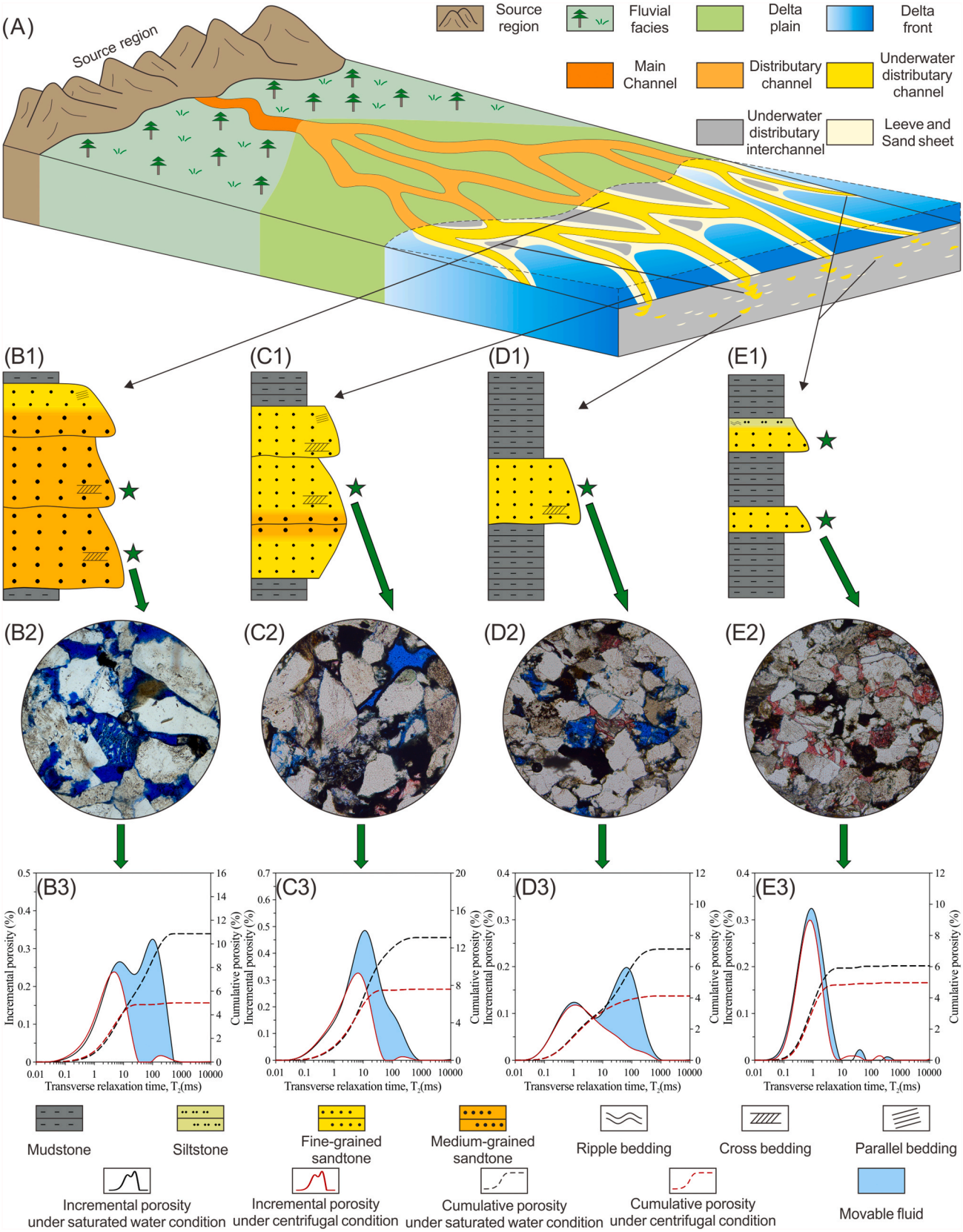

Fig. 16. The prediction model of fluid mobility in the lacustrine delta front setting. (A) Classic sketches of facies in the lacustrine delta sedimentary system. Four types of sandstone strata pattern: (B1) Medium-grained sandstone with thick bed, (C1) Fine-grained sandstone with thick bed, (D1) Fine-grained sandstone with medium bed, and (E1) Fine-grained sandstone with thin bed or located mudstone-rich sequence. (B2-E2) CTS images illustrating pore-throat types variation of four types of sandstone strata pattern. (B3-E3) The NMR T2 spectrum showing the fluid mobility variation of four kinds of sandstone strata pattern.

other emerging tight reservoir exploration areas.

Declaration of competing interest

The authors declare that they have no known competing financial interests or personal relationships that could have appeared to influence the work reported in this paper.

Data availability

Data will be made available on request.

Acknowledgments

We would like to thank the No.1 Oil Production Plant of PetroChina Changqing Oilfield Company for their support in sample collection, basic data, and core observation. This work was supported by the National Key R&D Program of China (Grant No. 2021YFA0719000).

References

Ajdukiewicz, J.M., Larese, R.E., 2012. How clay grain coats inhibit quartz cement and preserve porosity in deeply buried sandstones: observations and experiments. AAPG Bull. 96, 2091–2119.
Bjørlykke, K., 2014. Relationships between depositional environments, burial history and rock properties. Some principal aspects of diagenetic process in sedimentary basins. Sediment. Geol. 301, 1–14.
Brownstein, K.R., Tarr, C.E., 1979. Importance of classical diffusion in NMR studies of water in biological cells. Phys. Rev. Appl. 19, 2446–2453.
Cao, B., Luo, X., Wang, X., Zhang, L., Shi, H., 2023. Calcite-cemented concretions in non-marine sandstones: an integrated study of outcrop sedimentology, petrography and clumped isotopes. Sedimentology. 70, 1039-1074.
Clarkson, C.R., Freeman, M., He, L., Agamalian, M., Melnichenko, Y.B., Mastalerz, M., Bustin, R.M., Radliński, A.P., Blach, T.P., 2012. Characterization of tight gas reservoir pore structure using USANS/SANS and gas adsorption analysis. Fuel 95, 371–385.
Cui, H., Zhu, S., Wang, J., Gao, Y., Wan, C., Tong, H., 2022. Physical properties, pore-throat structure, fractal characteristics and their effects on the gas-bearing capacity of tight sandstone: a case study from the northern tianhuan depression, Ordos Basin, China. Nat. Resour. Res. 31, 1559–1584.
Dong, X., Meng, X., Pu, R., 2023. Impacts of mineralogy and pore throat structure on the movable fluid of tight sandstone gas reservoirs in coal measure strata: a case study of the Shanxi formation along the southeastern margin of the Ordos Basin. J. Pet. Sci. Eng. 220.
Dutton, S.P., Loucks, R.G., 2010. Diagenetic controls on evolution of porosity and permeability in lower Tertiary Wilcox sandstones from shallow to ultradeep (200–6700m) burial, Gulf of Mexico Basin. U.S.A. Mar. Petrol. Geol. 27, 69–81.
Gao, H., Li, H., 2015. Determination of movable fluid percentage and movable fluid porosity in ultra-low permeability sandstone using nuclear magnetic resonance (NMR) technique. J. Pet. Sci. Eng. 133, 258–267.
Hanson, A.D., Ritts, B.D., Moldowan, J.M., 2007. Organic geochemistry of oil and source rock strata of the Ordos Basin, north-central China. AAPG Bull. 91, 1273–1293.
Huang, H., Li, R., Chen, W., Chen, L., Jiang, Z., Xiong, F., Guan, W., Zhang, S., Tian, B., 2021. Revisiting movable fluid space in tight fine-grained reservoirs: a case study from Shahejie shale in the Bohai Bay Basin, NE China. J. Pet. Sci. Eng. 207, 109170.
Huang, H., Li, R., Xiong, F., Hu, H., Sun, W., Jiang, Z., Chen, L., Wu, L., 2020. A method to probe the pore-throat structure of tight reservoirs based on low-field NMR: insights from a cylindrical pore model. Mar. Petrol. Geol. 117, 104344.
Jia, C., Zheng, M., Zhang, Y., 2012. Unconventional hydrocarbon resources in China and the prospect of exploration and development. Petrol. Explor. Dev. 39, 139–146.
Jiang, F., Zhang, C., Wang, K., Zhao, Z., Zhong, K., 2019. Characteristics of micropores, pore throats, and movable fluids in the tight sandstone oil reservoirs of the Yanchang Formation in the southwestern Ordos Basin, China. AAPG Bull. 103, 2835–2859.
Jiang, M., Fang, H., Liu, Y., Zhang, Y., Wang, C., 2023. On movable fluid saturation of tight sandstone and main controlling factors —case study on the Fuyu oil layer in the Da'an oilfield in the Songliao basin. Energy 267.
Kenyon, W.E., 1992. Nuclear magnetic resonance as a petrophysical measurement. Nucl. Geophys. 6, 153–171.
Kleinberg, R.L., 1999. Nuclear magnetic resonance. In: Wong, P.-Z. (Ed.), Methods in the Physics of Porous Media. Academic Press, pp. 337–385.
Krakowska, P., Puskarczyk, E., Jędrychowski, M., Habrat, M., Madejski, P., Dohnalik, M., 2018. Innovative characterization of tight sandstones from Paleozoic basins in Poland using X-ray computed tomography supported by nuclear magnetic resonance and mercury porosimetry. J. Pet. Sci. Eng. 166, 389–405.
Lai, J., Wang, G., Cao, J., Xiao, C., Wang, S., Pang, X., Dai, Q., He, Z., Fan, X., Yang, L., Qin, Z., 2018a. Investigation of pore structure and petrophysical property in tight sandstones. Mar. Petrol. Geol. 91, 179–189.
Lai, J., Wang, G., Chen, J., Wang, S., Zhou, Z., Fan, X., 2017. Origin and distribution of carbonate cement in tight sandstones: the upper triassic Yanchang Formation chang 8 oil layer in west Ordos Basin, China. Geofluids 2017, 1–13.
Lai, J., Wang, G., Wang, S., Cao, J., Li, M., Pang, X., Zhou, Z., Fan, X., Dai, Q., Yang, L., He, Z., Qin, Z., 2018b. Review of diagenetic facies in tight sandstones: diagenesis, diagenetic minerals, and prediction via well logs. Earth-Sci. Rev.Earth Sci. Rev. 185, 234–258.
Lai, J., Wang, G., Wang, Z., Chen, J., Pang, X., Wang, S., Zhou, Z., He, Z., Qin, Z., Fan, X., 2018c. A review on pore structure characterization in tight sandstones. Earth-Sci. Rev.Earth Sci. Rev. 177, 436–457.
Li, A., Ren, X., Wang, G., Wang, Y., Jiang, K., 2015. Characterization of pore structure of low permeability reservoirs using a nuclear magnetic resonance method. Journal of China University of Petroleum (Edition of Natural Science) 39, 92–98.
Li, C., Liu, G., Cao, Z., Yuan, W., Wang, P., You, Y., 2019a. Analysis of petrophysical characteristics and water movability of tight sandstone using low-field nuclear magnetic resonance. Nat. Resour. Res. 29, 2547–2573.
Li, G., Liu, C., Zhou, Y.n., Wu, H., Awan, R.S., Shi, F., Wu, Y., Zang, Q., Wu, Y., 2023. Controlling effects of pore-throat structure and fractal characteristics on the physical properties of ultra-low permeability sandstone reservoirs: a case study of the sixth member of the Yanchang Formation in the Xiaojiahe area. Ordos Basin. Geol. J. 58, 1945–1964.
Li, P., Jia, C., Jin, Z., Liu, Q., Zheng, M., Huang, Z., 2019b. The characteristics of movable fluid in the Triassic lacustrine tight oil reservoir: a case study of the Chang 7 member of Xin'anbian Block, Ordos Basin, China. Mar. Petrol. Geol. 102, 126–137.
Li, Y., Fan, A., Yang, R., Sun, Y., Lenhardt, N., 2022. Braided deltas and diagenetic control on tight sandstone reservoirs: a case study on the Permian Lower Shihezi Formation in the southern Ordos Basin (central China). Sediment. Geol. 435, 106156.
Liu, G., Xie, S., Tian, W., Wang, J., Li, S., Wang, Y., Yang, D., 2022a. Effect of pore-throat structure on gas-water seepage behaviour in a tight sandstone gas reservoir. Fuel 310, 121901.
Liu, K., Wang, R., Shi, W., Travé, A., Martín-Martín, J.D., Baqués, V., Qi, R., Lin, J., Ye, H., 2022b. Diagenetic controls on reservoir quality and heterogeneity of the Triassic Chang 8 tight sandstones in the Binchang area (Ordos Basin, China). Mar. Petrol. Geol. 146, 105974.
Ma, B., Cao, Y., Eriksson, K.A., Wang, Y., 2019. Carbonate cementation patterns, potential mass transfer, and implications for reservoir heterogeneity in Eocene tight-oil sandstones, Dongying depression, Bohai Bay Basin, China: evidence from petrology, geochemistry, and numerical modeling. AAPG Bull. 103, 3035–3067.
Miocic, J.M., Girard, J.-P., Schöner, R., Gaupp, R., 2020. Mudstone/sandstone ratio control on carbonate cementation and reservoir quality in Upper Permian Rotliegend sandstones, offshore The Netherlands. Mar. Petrol. Geol. 115, 104293.
Morad, S., Al-Ramadan, K., Ketzer, J.M., De Ros, L.F., 2010. The impact of diagenesis on the heterogeneity of sandstone reservoirs: a review of the role of depositional facies and sequence stratigraphy. AAPG Bull. 94, 1267–1309.
Nelson, P.H., 2009. Pore-throat sizes in sandstones, tight sandstones, and shales. AAPG Bull. 93, 329–340.
Qiao, J., Zeng, J., Cai, J., Jiang, S., An, T., Xiao, E., Zhang, Y., Feng, X., Yang, G., 2021. Pore-scale heterogeneity of tight gas sandstone: origins and impacts. J. Nat. Gas Sci. Eng. 96, 104248.
Qin, Y., Yao, S., Xiao, H., Cao, J., Hu, W., Sun, L., Tao, K., Liu, X., 2021. Pore structure and connectivity of tight sandstone reservoirs in petroleum basins: a review and application of new methodologies to the Late Triassic Ordos Basin, China. Mar. Petrol. Geol. 129, 105084.
Qu, Y., Sun, W., Wu, H., Huang, S., Li, T., Ren, D., Chen, B., 2022. Impacts of pore-throat spaces on movable fluid: implications for understanding the tight oil exploitation process. Mar. Petrol. Geol. 137, 105509.
Schmitt, M., Halisch, M., Müller, C., Fernandes, C.P., 2016. Classification and quantification of pore shapes in sandstone reservoir rocks with 3-D X-ray micro-computed tomography. Solid Earth 7, 285–300.
Sen, S., Abioui, M., Ganguli, S.S., Elsheikh, A., Debnath, A., Benssaou, M., Abdelhady, A. A., 2021. Petrophysical heterogeneity of the early Cretaceous Alamein dolomite reservoir from North Razzak oil field, Egypt integrating well logs, core measurements, and machine learning approach. Fuel 306.
Shao, X., Pang, X., Jiang, F., Li, L., Huyan, Y., Zheng, D., 2017. Reservoir characterization of tight sandstones using nuclear magnetic resonance and incremental pressure mercury injection experiments: implication for tight sand gas reservoir quality. Energy Fuel. 31, 10420–10431.
Soeder, D.J., Chowdlah, P., 1990. Pore geometry in high and low-permeability sandstones, travis peak formation, east Texas. SPE form. Evaluation 5, 421–430.
Sun, Y., Deng, M., Ma, S., Chen, Y., Yu, L., Zhang, Y., Yan, B., Zhang, Y., 2015. Distribution and controlling factors of tight sandstone oil in Fuyu oil layers of Da'an area, Songliao Basin, NE China. Petrol. Explor. Dev. 42, 646–655.
Testamanti, M.N., Rezaee, R., 2017. Determination of NMR T2 cut-off for clay bound water in shales: a case study of Carynginia Formation, Perth Basin, Western Australia. J. Pet. Sci. Eng. 149, 497–503.
Thyne, G., 2001. A model for diagenetic mass transfer between adjacent sandstone and shale. Mar. Petrol. 18, 743–755.
Timur, A., 1969. Pulsed nuclear magnetic resonance studies of porosity, movable fluid, and permeability of sandstones. J. Petrol. Technol. 21, 775–786.
Vaisblat, N., Harris, N.B., Ayranci, K., Power, M., DeBhur, C., Bish, D.L., Chalaturnyk, R., Krause, F., Crombez, V., Euzen, T., Rohais, S., 2021. Compositional and diagenetic evolution of a siltstone, with implications for reservoir quality; an example from the Lower Triassic Montney Formation in western Canada. Mar. Petrol. Geol. 129, 105066.
Wang, F., Yang, K.U.N., Cai, J., 2018. Fractal characterization of tight oil reservoir pore structure using nuclear magnetic resonance and mercury intrusion porosimetry. Fractals 26, 1840017.

Wang, F., Zeng, F., 2020. Novel insights into the movable fluid distribution in tight sandstones using nuclear magnetic resonance and rate-controlled porosimetry. Nat. Resour. Res. 29, 3351–3361.
Wang, J., Wu, S., Li, Q., Xiao, S., 2020a. Controls of diagenetic alteration on the reservoir quality of tight sandstone reservoirs in the Triassic Yanchang formation of the Ordos Basin, China. J. Asian Earth Sci. 200, 104472.
Wang, Q., Chen, D., Gao, X., Wang, F., Li, J., Liao, W., Wang, Z., Xie, G., 2020b. Microscopic pore structures of tight sandstone reservoirs and their diagenetic controls: a case study of the Upper Triassic Xujiahe Formation of the Western Sichuan Depression, China. Mar. Petrol. Geol. 113, 104119.
Wang, W., Yue, D., Eriksson, K.A., Liu, X., Liang, X., Qu, X., Xie, Q., 2020c. Qualitative and quantitative characterization of multiple factors that influence movable fluid saturation in lacustrine deep-water gravity-flow tight sandstones from the Yanchang Formation, southern Ordos Basin, China. Mar. Petrol. Geol. 121, 104625.
Wang, Y., Gao, Y., Fang, Z., 2021. Pore throat structure and classification of Paleogene tight reservoirs in Jiyang depression, Bohai Bay Basin. China. Petrol. Explor. Dev. 48, 308–322.
Washburn, E.W., 1921. Note on a method of determining the distribution of pore sizes in a porous material. Proc. Natl. Acad. Sci. U.S.A. 115–116.
Wu, Y., Liu, C., Ouyang, S., Luo, B., Zhao, D., Sun, W., Awan, R.S., Lu, Z., Li, G., Zang, Q., 2022. Investigation of pore-throat structure and fractal characteristics of tight sandstones using HPMI, CRMI, and NMR methods: a case study of the lower Shihezi Formation in the Sulige area, Ordos Basin. J. Pet. Sci. Eng. 210, 110053.
Xi, K., Cao, Y., Liu, K., Jahren, J., Zhu, R., Yuan, G., Hellevang, H., 2019a. Authigenic minerals related to wettability and their impacts on oil accumulation in tight sandstone reservoirs: an example from the Lower Cretaceous Quantou Formation in the southern Songliao Basin, China. J. Asian Earth Sci. 178, 173–192.
Xi, K., Cao, Y., Liu, K., Wu, S., Yuan, G., Zhu, R., Zhou, Y., Hellevang, H., 2019b. Geochemical constraints on the origins of calcite cements and their impacts on reservoir heterogeneities: a case study on tight oil sandstones of the Upper Triassic Yanchang Formation, southwestern Ordos Basin, China. AAPG Bull. 103, 2447–2485.
Yang, Z., Wu, S., Zhang, J., Zhang, K., Xu, Z., 2022. Diagenetic controls on the reservoir quality of tight reservoirs in digitate shallow-water lacustrine delta deposits: an example from the Triassic Yanchang Formation, southwestern Ordos Basin, China. Mar. Petrol. Geol. 144, 105839.
Zang, Q., Liu, C., Awan, R.S., Yang, X., Li, G., Wu, Y., Lu, Z., Feng, D., 2022a. Occurrence characteristics of the movable fluid in heterogeneous sandstone reservoir based on fractal analysis of NMR data: a case study of the Chang 7 Member of Ansai Block, Ordos Basin, China. J. Pet. Sci. Eng. 214, 110499.
Zang, Q., Liu, C., Awan, R.S., Yang, X., Lu, Z., Li, G., Wu, Y., Feng, D., Ran, Y., 2022b. Comparison of pore size distribution, heterogeneity and occurrence characteristics of movable fluids of tight oil reservoirs formed in different sedimentary environments: a case study of the chang 7 member of Ordos Basin, China. Nat. Resour. Res. 31, 415–442.
Zhang, Q., Liu, Y., Wang, B., Ruan, J., Yan, N., Chen, H., Wang, Q., Jia, G., Wang, R., Liu, H., Xue, C., Liu, F., Yang, H., Zhu, Y., 2022a. Effects of pore-throat structures on the fluid mobility in chang 7 tight sandstone reservoirs of longdong area, Ordos Basin. Mar. Petrol. Geol. 135, 105407.
Zhang, Z., Li, Z., Deng, X., Liao, J., Zheng, X., 2022b. Multi-parameters logging identifying method for sand body architectures of tight sandstones: a case from the Triassic Chang 9 Member, Longdong area, Ordos Basin, NW China. J. Pet. Sci. Eng. 216, 110824.
Zou, C., Guo, Q., Yang, Z., Wu, S., Chen, N., Lin, S., Pan, S., 2019. Resource potential and core area prediction of lacustrine tight oil: the Triassic Yanchang Formation in Ordos Basin, China. AAPG Bull. 103, 1493–1523.
Zou, C., Zhang, G., Yang, Z., Tao, S., Hou, L., Zhu, R., Yuan, X., Ran, Q., Li, D., Wang, Z., 2013a. Concepts, characteristics, potential and technology of unconventional hydrocarbons: on unconventional petroleum geology. Petrol. Explor. Dev. 40, 413–428.
Zou, C.N., Yang, Z., Tao, S.Z., Yuan, X.J., Zhu, R.K., Hou, L.H., Wu, S.T., Sun, L., Zhang, G.S., Bai, B., Wang, L., Gao, X.H., Pang, Z.L., 2013b. Continuous hydrocarbon accumulation over a large area as a distinguishing characteristic of unconventional petroleum: the Ordos Basin, North-Central China. Earth-Sci. Rev.Earth Sci. Rev. 126, 358–369.